Doctoral Dissertation

Development of Water Surface Reflection/Refraction Correction Techniques for UAV-Based Photogrammetry of Shallow Water Bottom

浅水底の UAV 写真測量のための水面反射・屈折補正技術の開発

September, 2018

I GD Yudha Partama

Graduate School of Science and Engineering

Yamaguchi University

Acknowledgement

This study would not be possible without the “Beasiswa Unggulan” scholarship from the Ministry of Education and Culture (Indonesia) granted to me from September 2015 to September 2018, for which I am very grateful.

Firstly, I would like to express my sincere gratitude to my supervisor, Associate Professor Ariyo Kanno for the continuous support of my Doctoral study and related research, for his patience, motivation, and immense knowledge. His guidance helped me in all the time of research and writing of this thesis. I could not have imagined having a better advisor and mentor for my Doctoral study.

Besides my supervisor, I would like to thank the rest of Professors in “Eisei Laboratory”: Prof. Masahiko Sekine, Prof. Tsuyoshi Imai, Prof. Takaya Higuchi, and Associate Professor Koichi Yamamoto, for their insightful comments and encouragement, but also for the hard question in the regular English and Literature seminar which incented me to widen my research from various perspectives. My sincere thanks also goes to Professor Tasuku Tanaka and Proffesor Takahiro Osawa that give me the opportunity to come to Yamaguchi University.

I thank my fellow labmates in for the stimulating discussions and for all the fun we have had in the last three years; Riza, Kagawa, Minamata, Miyazaki, Dyah, Vita, Atin, Mai, Wang, Tape, Pure, and Art and all friends who already graduated earlier. The CRESSOS student in Yamaguchi University that all give me much help: Sudi, Tiwi, Edi, Husnia and Sena. All Indonesian friends who studying together at Yamaguchi University. Life won’t be fun with them.

Last but not the least, I would like to thank my family: my parents, my sister and my big families for supporting me physically and spiritually throughout my study, writing this thesis and my life in general. Especial thank goes to my beloved wife Diah Dirma for the patient and support.

Summaries

Shallow-water bathymetric data are important in a wide range of applications. In river systems, these data are important in management and research applications such as river hydrodynamic modeling and investigation of bank erosion and morphological change. In coastal settings, these data are fundamental to the study and management of coral reefs and estuarine ecosystems because water depth distribution governs the physical and biological characteristics (e.g., flows, waves, and benthic habitats). However, in shallow water areas such as coral reefs and river channels, there is no perfect method for exhaustive bathymetric mapping. Conventional ship sounding is constrained by ship access. Single-beam echo-sounding from boat is time consuming to survey a wide area. Airborne light detection and ranging (LiDAR) is too costly to a wide area.

To supplement these approaches, the recent development of Structure-from-Motion (SfM) and Multi-view Stereo (MVS) photogrammetry technique, has been proposed. This technique greatly reduces the level of expertise and ability required to extract high resolution and accurate bathymetric data, using cheap consumer-grade digital cameras mounted on small Unmanned Aerial Vehicles (UAVs) (e.g. drones). However, the applicability of this technique is limited by water surface refraction/reflection effects. The refraction effect caused the submerged areas record shallower water depths than the reality. In addition, the reflection effect hinders the matching between images and makes the point-cloud density and accuracy insufficient. Therefore, the methods to correct these effects are required.

The primary objectives of this thesis were to develop the practical methods to remove the water-surface refraction/reflection effects for UAV-based shallow-water photogrammetry. In the first part of this study, an empirical method was presented to correct for the effect of refraction after the usual SfM-MVS photogrammetry processing. The presented method utilizes the empirical relation

between the measured real-scale depth and the estimated apparent depth at some submerged points. Specifically, an empirical correction factor is derived by least-squares method and is used to convert the apparent water depth into a refraction-corrected (real-scale) water depth. To examine its effectiveness, this method was applied to two river sites, and compared the root mean square error (RMSE) in the corrected bottom elevations with those obtained by three existing methods. The result shows that the presented method is more effective than the two existing methods: The method without applying correction factor and the method utilizes the refractive index of water (1.34) as correction factor. In comparison with the remaining existing method, which used the additive terms (offset) after calculating correction factor, the presented method performs well in Site 2 and worse in Site 1. Overall, the accuracy of the method depends on various factors such as the locations, image acquisition, and Global Positioning System (GPS) measurement conditions. The most effective method can be selected by using statistical selection (e.g. leave-one-out cross validation).

In the second part of this study, a new imaging technique was presented to suppress the effect of the water-surface reflections in the image retrieval step. In this technique, first, the drone was ordered to take a short video instead of a still picture at each waypoint. Second, the motion stabilizer was performed to remove the effects of the displacement and rotation of the camera in each video, caused by the movement of the UAV during the recording. Finally, two sets of input images were generated from each video for the SfM-MVS procedure. One set was generated by randomly selecting one frame from each video, in order to simulate an image obtained by normal photography. The other set of images was generated by applying a temporal minimum filter (a filter that extracts the smallest RGB value for each pixel from the available video frames) to the video, in order to reduce the effect of reflection.

In order to assess the effectiveness of this method, it was tested in three experiments in a river and at the coast, and compared the density, accuracy and precision of point-cloud as well as the accuracy and precision of bathymetric map with those generated from a randomly chosen frame. The results showed that the

presented technique increased the overall density of the point cloud by factor of 3.6, 1.8, and 3.2 at Site 1, 2, and 3, respectively. In addition, the local point density increased in most parts of the submerged region upon of the presented technique by increasing the number of matching points between images in the MVS algorithm. The presented technique also showed better accuracy and precision in determining the water bottom elevation in point clouds. On the other hand, the error statistics of the bathymetric map show that the RMS error decreased by factor 3.8, 2.9, and 2.5 at Site 1, 2, and 3, respectively, upon application of the presented technique. In summary, the presented technique improves the point cloud density, accuracy and precision of UAV-based shallow-water photogrammetry by reducing the effects of water-surface reflection.

List of Abbreviation

CF	Correction Factor
DEM	Digital Elevation Model
DSM	Digital Surface Model
GCP	Ground Control Point
GNSS	Global Navigation Satellite System
GPS	Global Positioning System
LiDAR	Light Detection and Ranging
MAE	Mean Absolute Error
ME	Mean Error
MVS	Multi-view Stereo
PNG	Portable Network Graphics
RMSE	Root Mean Square Error
RMSR	Root Mean Square Residuals
RTK-GPS	Real Time Kinematic-Global Positioning System
SfM	Structure-from-Motion
SIFT	Scale Invariant Feature Transform
TIN	Triangulated Irregular Network
TMF	Temporal Minimum Filter
TST	Total Station Theodolite
UAV	Unmanned Aerial Vehicle
sUAV	Small Aerial Vehicle
WSE	Water Surface Elevation

List of Contents

List of Figures

List of Tables

Chapter 1. Introduction

1.1. Background

Shallow-water bathymetric data are plays an important role in various management and research works. In coastal marine settings, especially in coral reef system, this data is a key element of biological oceanography. The depth and characteristics of the shallow-water bed define the habitat for benthic organisms, and are fundamental parameters of coral reef ecosystems. In river systems, these data are important in management and research applications such as the identification of river hydro-morphological features (Monica et al., 2015), investigation of bed deformation and bank erosion (Nagata et al., 2000), and assessment of river habitat quality (Ulrich et al., 2004).

Traditionally, these data were obtained mainly by on-site surveying techniques such as ground-based measurement using tape measures, levelling equipment and global positioning systems (GPS) devices. However, these techniques are time consuming, and labour intensive, and are therefore often limited in spatial coverage. Furthermore, these techniques only provide the measurements of depth at specific points, rather than giving continuous coverage.

Recently, the use of airborne light detection and ranging (LiDAR) bathymetric systems has provided a new approach for mapping shallow-water topography with capable of measuring maximum water depth of up to three times the Secchi depth in clear water, and up to two times in more turbid waters (Feurer et al., 2008 & Marcus, 2012). However, this approach suffers from a lack of reliability in shallow waters (water depths < 0.3 m) due to the difficulty of the separation reflectance signals from the water surface and the bottom bed (Feurer et al., & Marcus, 2012). In addition, this approach is severely limited by high cost, restricted sensor availability, and coarse spatial resolution and a lack of reliability in shallow water areas.

The use of maritime vessels to carry out multi-beam bathymetric survey is time consuming and constrained by ship access in the shallow water areas. Single-beam echo-sounding from small boat is limited by its small spatial footprint on the sea/river bed. Overall, in shallow water areas such as river channels and coral reefs, there is no perfect method for exhaustive bathymetric mapping.

As complementary methods of carrying out bathymetry in these areas, aerial photogrammetry based on stereoscopic imagery, which is a classical surveying method has been employed to provide high-resolution spatial bathymetric models (Tewinkel, 1963; Fryer, 1983; Fryer and Kniest, 1985; Westaway et al., 2000, 2001; Murase et al., 2008). Previously, Tewinkel (1963), Westaway et al. (2000 and 2001), and Murase et al. (2008) proposed various methods for water surface refraction correction. Further, Fryer (1983) proposed a practical solution for detailed bathymetric mapping in shallow water using a floating camera platform. In addition, Fryer and Kniest (1985) examined the magnitudes and distributions of depth errors caused by waves. The recent development of Structure-from-Motion (SfM) and Multi-view Stereo (MVS) methods has enabled semi-automatic measurement of bathymetry from aerial images taken by consumer-grade digital cameras mounted on unmanned aerial vehicles (UAVs) (Woodget et al., 2015; Casella et al., 2016; Dietrich, 2016; Partama et al., 2017).

The applicability of this method is limited by water surface refraction and reflection effects. The refraction effect causes in-water measurements to be appearing shallower. Without the application of a correction procedure, the refraction problem results in the overestimation of true bed elevation (i.e. an underestimation of water depth) and reduce the accuracy of UAV-based shallow-water photogrammetry (Fryer, 1983; Fryer and Kniest, 1985; Butler et al., 2002; Westaway et al., 2001). A simple refraction correction method has been developed by (Westaway et al., 2001). This method proposes using the refractive index of water (1.34) as the CF to convert the apparent water depth into real water depth. This CF is the minimum possible value that can be used when the refraction effect is very low (i.e. camera position at the nadir of the target points). It can be shown

geometrically that this correction factor is not always the optimal one, as shown in the case of two cameras by Murase et al., (2008) and Kanno et al., (2017). According to Murase et al., (2008) and Kanno et al., (2017), the correction factor varies depending on the position of the two cameras relative to the target points. However, in real underwater photogrammetry, it is not feasible to calculate the geometrical CF for two reasons: 1. No researcher has derived the geometrical CF for cases with more than two views. 2. Common photogrammetry software does not output the information on which camera was used for estimating the coordinates of each point (in the dense point cloud), which is required for calculating the geometrical CF. In this study, I present an empirical method based on the least-square method that estimates a reasonable CF for a specific flight by minimizing the root mean square error (RMSE) in the refraction-corrected bottom elevation.

The reflections effect causes the point-cloud density and accuracy of UAV-based shallow-water photogrammetry insufficient because this effect hinders the matching between images in SfM process (Dietrich, 2016; Casella et al., 2016). Some work has been done to overcome this problem. The water-surface reflection effect can be reduced by carefully designing the flight plan (Dietrich, 2016; Casella et al., 2016). However, this method cannot be applied in all atmospheric conditions (e.g., on cloudy days), which limits the surveying time. Westaway et al. (2001) corrected for water-surface reflection by manually eliminating the point clouds in which the photogrammetry was assumed to have not detected the bottom. However, this method may only be applied when the reflection on the water surface is insignificant and the areas that contain the reflection are very small. Dietrich et al., (2017) suggested another method to minimize the reflections effect by equipping the UAV's camera with a polarizing filter. However, the effect of polarizing filter in reducing the reflection effect is not uniform across the whole frame of imagery. In this study, I present a new imaging technique to supress the effect of water surface reflection by applying a temporal minimum filter to the videos taken by cameras mounted on UAV. This filter extracts the smallest RGB

value of each pixel between video frames and composed an image with greatly reduce water surface reflection effect.

1.2. Objectives of this thesis

The primary objectives of this thesis were to develop the practical methods to correct the water surface refraction and reflection effects for shallow-water bathymetric mapping using UAV-photogrammetry, and to evaluate the results against those from existing approaches. Within each of these specific chapters, the following research questions are posed;

1. Development of water surface refraction correction method (Chapter 3)
    - How do the results (accuracy and precision of the refraction-corrected bottom elevation) of the presented method compare with those obtained using three existing methods: a) without applying correction factor; b) with apply the refractive index of water (1.34) as correction factor; and c) with apply the linear correction (Least-square) method which estimate the gain (CF) and offset simultaneously? Do these measures vary between different field sites?
    - How does the relation between the noise variations contain in the apparent water depth with the variation of the correction factor?
2. Development of water surface reflection correction method (Chapter 4)
    - How do the results (density, accuracy and precision of point clouds) of the presented method compares with a randomly chosen frame (simulating the still photograph)? Do these measures vary between different field sites?
    - How do the results (accuracy and precision of bathymetric map) of the presented method compares with a randomly chosen frame (simulating the still photograph)? Do these measures vary between different field sites?

1.3. Thesis structure

This thesis comprises four chapters. The following paragraphs provide an overview of each chapter.

Chapter 1 describes the background, objectives, and the nature of the research presented in subsequent chapters.

Chapter 2 provides the outline of UAV-based shallow-water photogrammetric mapping. This chapter includes the UAV and SfM-photogrammetry theory, general workflow of SfM-MVS photogrammetry processing, and the existing of water surface refraction/reflection correction methods.

Chapter 3 is focussed on developing a new method to correct the water surface refraction effect for UAV-based shallow-water photogrammetry by using empirical linear regression (Least-square) method. The effectiveness of this proposed method through its application to two river sites was tested. The accuracy and precision in the corrected bottom elevation were compared with those from three other existing methods. In addition, the relationship between the correction factor and the noise contain in the estimated apparent water depth was investigated.

Chapter 4 is focussed on developing a new method to correct the water-surface reflection effect for UAV-based shallow-water photogrammetry. In this method, a new imaging technique was proposed to supress the effect of reflection by applying a temporal minimum. To examine the performance of this method, it was tested at three small shallow-water sites. The density and accuracy of point clouds as well as the accuracy of bathymetric map generated by using this method were examined, and compared with simulated randomly chosen frame (simulating still photograph).

Chapter 5 draws together the major findings from each chapter and provides an overarching evaluation of the proposed methods for water surface refraction/reflection correction in UAV-based shallow-water

photogrammetry. This chapter also makes suggestions for further research.

1.4. Publications

1. 掛波優作, 神野有生, 赤松良久, **I. G. Y. Partama**, 乾隆帝. (2016). UAV-SfM 手法を用いた高解像度かつ簡便な河道測量技術の検証. 河川技術論文集. Vol.22, pp.79-84. (Printed)
2. 神野有生, 赤松良久, **I. G. Y. Partama**, 乾隆帝, 後藤益滋, 掛波優作. (2017). 論文題目：UAV と SfM-MVS を用いた河道水面下測量技術における水面屈折補正の高度化. 河川技術論文集. Vol.23, pp.185-190. (Printed)
3. **I. G. Y. Partama**, A. Kanno, Y. Akamatsu, R. Inui, M. Goto, and M. Sekine. (2017). A Simple and Empirical Refraction Correction Method for UAV-Based Shallow-Water Photogrammetry. proceeding of ICPRS 2017: 19th International Conference on Photogrammetry and Remote Sensing. Kyoto Japan, pp.2778-2785. (Printed)
4. **I. G. Y. Partama,** A. Kanno, M. Ueda, Y. Akamatsu, R. Inui, M. Sekine, K. Yamamoto, T. Imai, and T. Higuchi. (2018). Removal of Water-Surface Reflection Effects with a Temporal Minimum Filter for UAV-Based Shallow-Water Photogrammetry. DOI:10.1002/esp.4399. (Accepted; In Production)
5. 神野有生, 米原千絵, I. G. Y. Partama, 小室隆, 乾 隆帝, 後藤益滋, 赤松良久. (2018). UAV と SfM-MVS を用いた河床冠水部の写真測量のための水面屈折補正係数に関する検討. 河川技術論文集. Vol. 24, pp. 19-24. (Printed)

Chapter 2. UAV-Based Photogrammetry of Shallow-Water Bottom

2.1. Unmanned Aerial Vehicle (UAV)

Small aerial platforms have already been used in geosciences several years ago for small format aerial photography. UAVs can be used for area coverage between square meters and several hectares and thus can help to close the gap between terrestrial imaging utilisation covering small areas (sub-m^2) and manned aircraft image covering large areas (many km^2) (Eisenbeib, 2009). Furthermore, the temporal scale can be approached from a new perspective, as well, because flexible data acquisition enables observation of high temporal frequency. The advanced technology, especially in recent years, allow to easy handle and low-cost (compared to manned aircraft) flying device, which has increased the recognition of the potential of UAVs for earth surface observations (Carrivick et al., 2013). In the field of remote sensing, most of the systems used are mini-UAVs with a digital camera for aerial photography. Images from the digital camera provide accurate data that can be processed with existing methods and algorithms into point clouds and surface models for further use.

In larger scale campaigns, the multiple flights have to be undertaken and even then, the areas that can be covered are limited to a few hectares, especially in the case of rivers with forested banks, where line-of-sight can be quite limited. Other challenges may include flight time, payload capacity, reliability, and weather conditions. The flight time and payload capacity of the UAV are not typically a serious problem in photogrammetric use, as digital cameras can be very light. However, if higher grade cameras, such as full-frame digital single-lens reflex cameras (DSLR) are to be used, the UAV also needs to be larger in order to be able to carry the camera and provide long enough a flight time.

2.2. Structure-from-motion photogrammetry (SfM)

In particular, a method known as 'Structure from Motion' has been gaining popularity in recent years. The SfM approach essentially provides an automated image matching method for generating the relative 3D geometry of a scene from a series of overlapping 2D images, which may then be georeferenced to map co-ordinates. The algorithms used differ from those employed within traditional photogrammetry in that they allow the collinearity equations to be solved and the relative scene geometry to be constructed without prior knowledge of camera positions or the use of ground control points (GCPs) (Westoby et al., 2012, Fonstad et al., 2013). The SIFT (scale invariant feature transform) algorithm developed by Lowe. (2004) is one of the image matching algorithms frequently used as part of the SfM process and is a powerful method capable of recognising conjugate (matching) points in overlapping images regardless of changes in image scale, view angle or orientation (Fonstad et al., 2013). This is performed using patterns of image brightness and colour gradients (i.e. variations in image texture) which can be identified at various different scales, and represents a significant advantage for use with UAV imagery. The kernel or area-based approaches used in traditional photogrammetry require constant image resolution and the acquisition of imagery at nadir, which is difficult to obtain using the less stable UAS platforms (Rosnell and Honkavaara, 2012, Turnel et al., 2012, Fonstad et al., 2013).

The SfM process allows the identification of prominent matching points between convergent overlapping images and successive least squares bundle block adjustments are then used to estimate the camera parameters, relative camera positions, and the scene geometry. This process aligns the separate input images and outputs a model of the scene geometry as a set of sparse data points, known as a 'point cloud' (Neitzel and Klonowski, 2011, Harwin and Lucieer, 2012). During this phase, automated camera lens calibrations are also conducted. These self-calibrations help to reduce the impact of lens distortion on the resulting model. Following the generation of the sparse point cloud, multi-view stereo techniques are used to revisit the original images and densify the point cloud. This step is particularly memory intensive.

At this stage in the process, camera positions are known only in relative space and the GCPs locations have not yet been specified. As a result, the point cloud is generated in an arbitrary image-space co-ordinate system (Harwin and Lucieer, 2012, Turner et al., 2012, Verhoeven et al., 2012, Westoby et al., 2012), and must be georeferenced to an absolute co-ordinate (World coordinates) system to be useful for quantitative topographic studies. Georeferencing is typically performed using one of two approaches:

- Direct georeferencing. This makes use of image acquisition locations collected with the on-board GPS during flight (Neitzel and Klonowski, 2011, Harwin and Lucieer, 2012, Turner et al., 2012). Such information is not always available, and for imagery collected from UAS often has a relatively low spatial accuracy (in the order of a few meters). As a result, this approach does not always produce the most accurately positioned output (Turner et al., 2012)
- Indirect georeferencing. This approach is carried out using the known positions of GCPs, which are used to perform the three-dimensional, seven parameter transformations (Verhoeven et al., 2012, Westoby et al., 2012). GCPs may be fixed features of known position within the imagery, or artificial targets distributed within the area of interest whose position is accurately surveyed. A minimum of three GCPs are required for a successful transformation (Verhoeven et al., 2012).

These methods both provide a linear transformation of the point cloud and any errors will be carried through to the final georeferenced output (Fonstad et al., 2013). Once transformed into real-world co-ordinates using one of these methods, the point cloud may be exported as a rasterised digital elevation model (DEM) or textured using the original imagery to given an orthophoto. Further detail on the SfM process is provided in Section 2.3.

2.3. Structure-from-motion processing

The processing of imagery collected at all sites was carried out in a widely used SfM-MVS commercial software package, Agisoft PhotoScan Professional version 1.2.6. to 1.3.4. This software package contains the necessary routine required to output 3D sparse and dense point, rasterised DEMs and orthomosaics from the raw UAV imagery. The workflow is summarised in Figure 2-1. This section does not provide a detailed mathematical explanation of the SfM-MVS process, but instead aims to present an overview of each step and highlight the advantages of the approach for processing imagery acquired from a UAV.

2.3.1 Image import

The process commences with the straightforward uploading of images into the PhotoScan software.

2.3.2 Image alignment

The image alignment stage involves the use of advanced pattern matching algorithms to identify features that are present in a number of overlapping images (i.e. the same real-world features in multiple images). These 'features' are patches of distinctive image textures which are most prominent within the image dataset (James and Robson, 2012). The algorithms used in the PhotoScan software to match these image features are thought to be similar to the SIFT proposed by Lowe (2004), but the full details are not publically available. Such algorithms do not rely on the area-based cross-correlation strategies typically used in standard photogrammetry, which establish conjugate point matches by maximising the correlations between image sub-regions (or templates) and as a result are highly sensitive to differences in scale, orientation and illumination.

In contrast, the SfM algorithms instead rely on the detection of local image gradients at multiple scales. A hierarchical system is implemented, whereby the image dataset is separated into small groups which are each assessed for successful point matches. The camera parameters, camera orientations and scene

geometry are computed for each of these small groups using successive least squares bundle adjustments. The separate groups are then gradually aggregated to create the complete geometric scene. This process allows sub-pixel matching accuracy with invariance to scale, orientation and illumination (Lowe, 2004, Snavely et al., 2008). The image alignment settings used for each survey were as follows:

- Accuracy: Highest.

  The "highest" accuracy setting uses images upscale by factor of 4.

  The "high" accuracy setting uses the original images.

  As a result, the higher the accuracy setting, the greater the processing time, but this results in more accurate camera positioning.
- Pair preselection: Generic.

  This setting helps to speed up the alignment process by finding overlapping images by matching downscaled images first, and then performing the full scale image alignment using pairs of the original images (Agisoft, 2017).

This process results in the estimating of the camera's intrinsic and extrinsic parameters, as well as the coordinates of the sparse point clouds. The point clouds for each survey were manually edited to remove the obviously erroneous points. Manual editing has clear limitations in terms of user subjectivity and lack of exact repeatability, but provides a rapid approach for the removal of outliers.

2.3.3 Georeferencing

In order to be useful for quantitative measurement of underwater topography, the geometric model (associated with point cloud) needs to be scaled, translated and rotated into a relevant geographic coordinate system. This was implemented using an indirect approach and linearly transformed using seven rigid parameter transformations, consisting of three translation parameters in X, Y, and Z, three rotation parameters around X-axis, Y-axis and Z-axis, and one scale parameter which applies to all three dimensions. These transformation parameters were calculated by relating the position of the GCPs in the geometric

model to their real-world coordinates. The positions of the GCPs for each survey were identified visually on the geometric model and their positions checked on the original input imagery. Further, their associated X, Y, and Z coordinates (as measured in the field) were imported into PhotoScan and used to derive the relevant transformation parameters and georeferenced the model by using least square method. In theory this process requires a minimum of just three GCPs (James and Robson, 2012). In practice, more GCPs will produce a better model registration, but it has not yet been firmly established what the optimum number of GCPs is or how they should be distributed for use within a UAV-SfM workflow.

2.3.4 Optimization

The linear rigid-body transformation (least square) used in the georeferencing phase does not remove any non-linear component, this usually caused the non-linear deformations in the model. Such deformation can be removed by applying the optimization procedure. This process is usually based on the weights of the camera, marker and projection accuracy values specified by the user (below) (Agisoft, 2017). During this process, PhotoScan adjusts estimated point coordinates and camera parameters minimizing the sum of re-projection error and reference coordinate misalignment error (Agisoft, 2017). The following settings were used within the optimisation process for all datasets;

- Camera accuracy: 10 m.

  This value provides an estimate of how accurately the position of the camera used in this project. This setting was the default option and the other settings were not explored within this project.

- Marker accuracy: 0.1 m.

  This was a conservative estimate based on limited knowledge at the time of processing. Recent updates to the PhotoScan user manual suggest that if GCPs are to be used in the optimisation process (as they are here), then marker accuracy should be set at zero.

- Projection accuracy: 0.1 pixels.

This value provides an estimate of how accurately the markers have been placed on the imagery. At the time of processing a setting of 0.1 was the default option and other settings were not explored within this project.

2.3.5 Dense point cloud generation

PhotoScan allows generating a dense point cloud model. Based on the estimated camera positions, the program calculates depth information for each camera to be combined into a single dense point cloud (Agisoft, 2017). The process uses a multi-view stereo-reconstruction on the pixel values of the aligned images (Verhoven, 2012). The following settings were used for each dataset;

- Quality: Ultra High.

  Higher quality settings can be used to obtain more detailed and accurate geometry, but they are require longer time for processing.

  The "Ultra High" accuracy setting uses the original images.

- Depth filtering modes: Mild.

  PhotoScan has several built-in filtering algorithms to sort out the outliers in the dense point cloud.

  The "Mild" depth filtering mode setting is recommended for aerial data processing with contain meaningful small details. In this setting, the important features will not be sorted out as outliers.

  The "Aggressive" depth filtering mode setting is recommended for aerial data processing with does not contain meaningful small details. This setting may sort out most of the outliers.

  The "Moderate" depth filtering mode brings results that are in between the Mild and Aggressive approach.

2.3.6 Export

At the end of the SfM-MVS workflow, the automated export function in PhotoScan software was used to output the 3D point clouds, orthophoto and DEMs for each site.

1. INPUT: Image dataset
High level of overlap between images

2. PROCESS: Image alignment
Matches features using SIFT algorithms (or similar), computes camera intrinsic & extrinsic parameters

3. OUTPUT: Sparse point cloud

4. PROCESS: Georeferencing & image alignment optimization

5. PROCESS: Multiview Stereo-reconstruction
Densification of the point cloud

6. EXPORT: Dense point cloud, orthophoto, and DEM

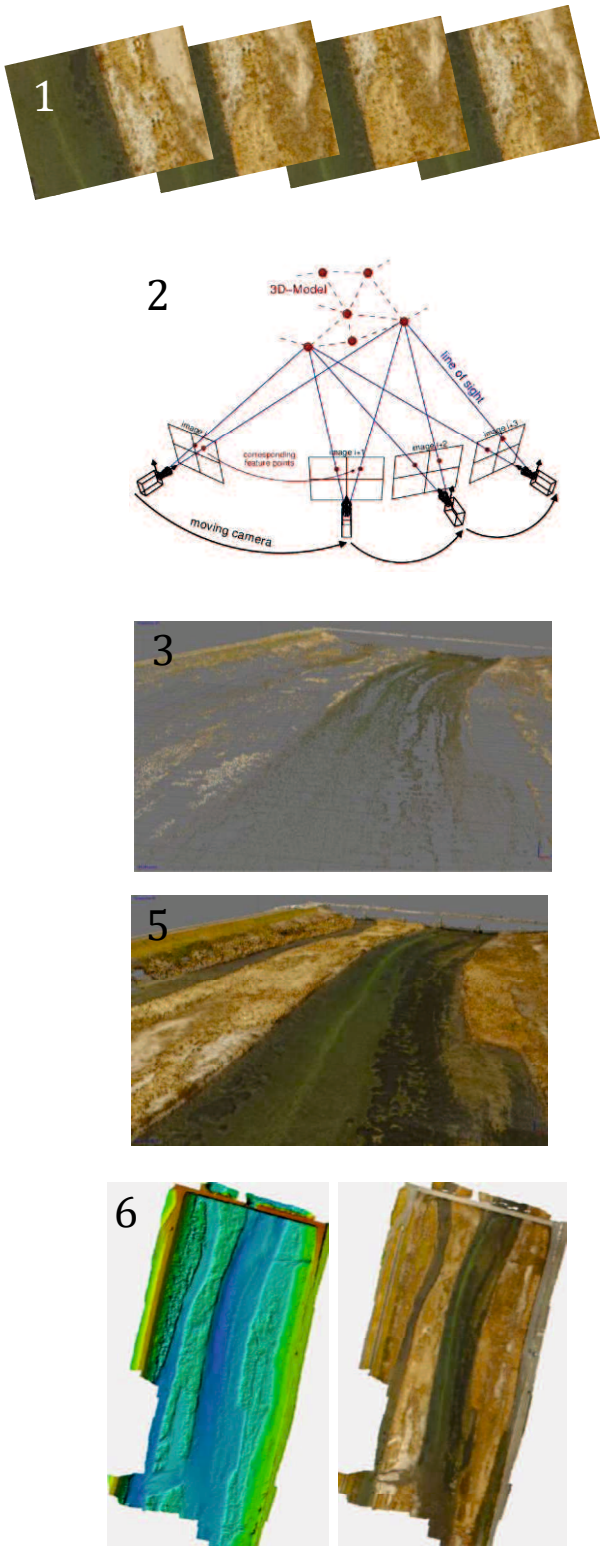

Figure 2-1. Overview of the SfM-MVS process, as implemented using the Agisoft PhotoScan Pro software.

2.4. UAV-based photogrammetry of shallow water bottom

An explosion in the use of SfM photogrammetry in geomorphology and the rapid growth of consumer-grade, small unmanned aerial vehicles (sUAV) provide another approach for collecting high-resolution bathymetric data via optical remote sensing. Photogrammetry, both traditional stereo and multi-view stereo, offers a way to measure shallow water bathymetry directly in clear water systems. So called through water, or two-media photogrammetry, has a relatively long history (Tewinkel, 1963; Harris and Umbach, 1972; Fryer and Kniest, 1985; Westaway et al., 2000, 2001; Butler et al., 2002; Murase et al., 2008; Lane et al., 2010; Woodget et al., 2015). The major limitations of this technique are that in water measurements are affected by refraction and reflection effects. Several methods have been proposed to overcome these problems. Details of the existing methods for water surface refraction and reflection correction are described in the following sections.

2.4.1 The existing of water surface refraction correction methods

Underwater topography which is acquired by through water photogrammetry is affected by light refraction so the resultant of water bottom elevation is higher than its true value. The geometry of the refraction of light as it passes through the air-water interface is described by Snell's Law (Equation 2-1) and shown in Figure 2-2:

$$\frac{\sin r}{\sin i} = \frac{h}{h_A} = \frac{n_1}{n_2} \qquad \text{Equation (2-1)}$$

Where r is the angle of refracted light ray above the water surface, i is the angle of the incident light ray originating from below water surface, h is true depth, h_A is apparent depth, n_2 is the refractive index of air (which has value of 1) and n_1 is refractive index of water (which has value 1.34 for clear water).

A. Geometrical correction method

A geometrical correction method was tested by Westaway et al., (2001), where the exact camera positions were taken into account (Figure 2-2 and Equation 2-3). However, this geometrical correction method is only considering single view camera case, which is not feasible to apply for multi-view case in SfM-MVS process.

$$r = tan^{-1}\frac{D}{dH} \qquad \text{Equation (2-2)}$$

$$h = \frac{x}{\tan i} = \frac{h_a * \tan r}{\tan\left[sin^{-1}\left(\frac{n_2}{n_1} * sinr\right)\right]} \qquad \text{Equation (2-3)}$$

$$CF = \frac{h}{h_a} = \frac{\tan r}{\tan\left[sin^{-1}\left(\frac{n_2}{n_1} * sinr\right)\right]} \qquad \text{Equation (2-4)}$$

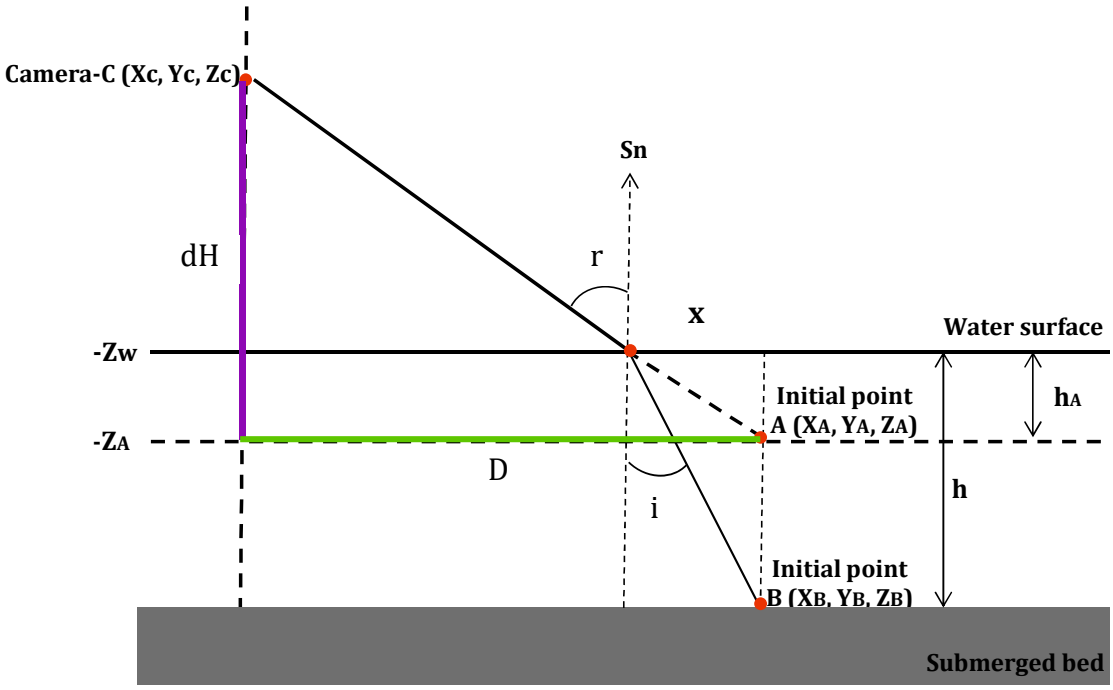

Figure 2-2. Relationship between camera location, water surface elevation, apparent water depth, and actual water depth (Westaway et al., 2001).

The more simple correction procedure was established by Westaway et al., (2000) and followed by Woodget et al., (2015). In this correction method, the corrected depth (h) is calculated by multiplied the apparent depth (h_A) with the refractive index of water (n_1), as shown in Equation 2-2.

$$h = n_1 \, x \, h_A \qquad \text{Equation (2-5)}$$

This simple correction method requires the imagery acquired from vertical view angles (nadir) and the submerged bed must be visible. The resultant of corrected bottom elevation produced using this method were found to have levels of accuracy and precision commensurate to those produced for exposed topography in areas of shallow water (i.e. depths <0.4m). However this correction factor (CF = 1.34) is the minimum possible value that can be used when the refraction effect is very low (the incidence angle is very small), as shown in Figure 2-3 (Westaway et al., 2001). On the other hand, based on the two-view case of geometrical refraction correction method proposed by 神野有生., (2017), the CF varies depending on the position of the two cameras relative to the target point (Figure 2-4).

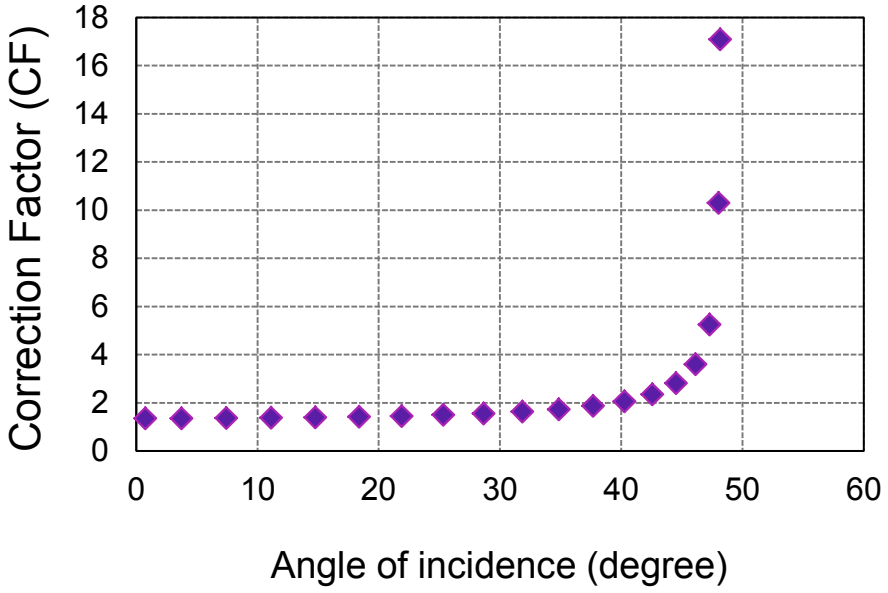

Figure 2-3. Relationship between incidence angle and correction factor derived from single view case (Equation2-4) of geometrical refraction correction method (Westaway et al., 2001).

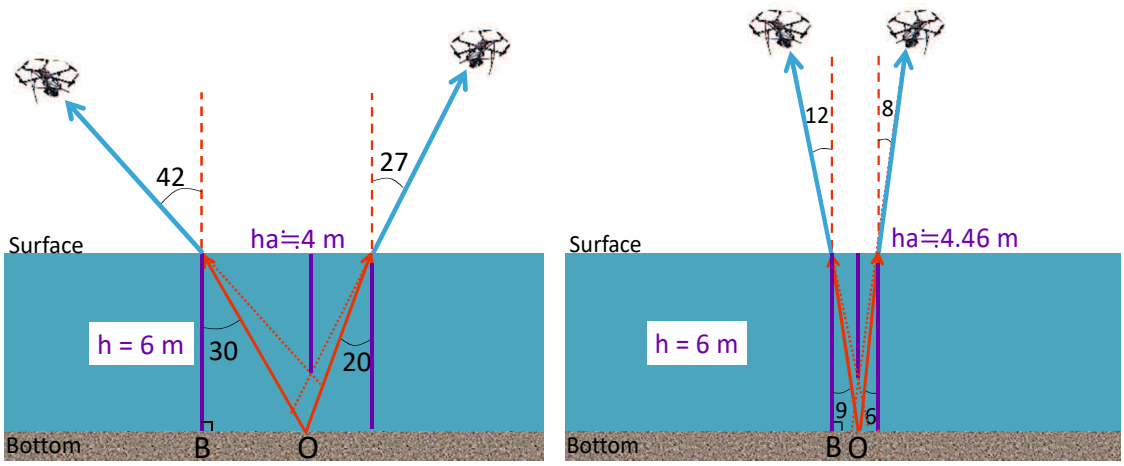

(a) Correction factor (h/ha) ≒ 1.50 (b) Correction factor (h/ha) ≒ 1.34

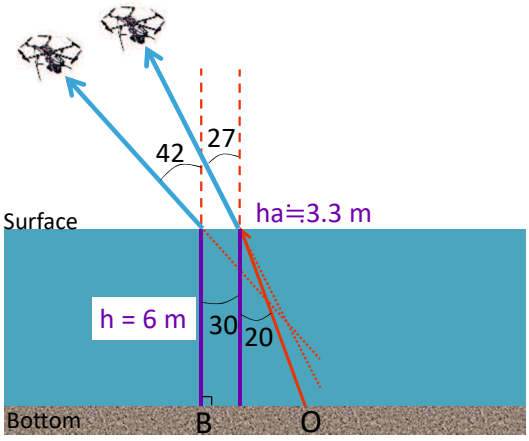

(c) Correction factor (h/ha) ≒ 1.82

Figure 2-4. Correction factor derived from two-view case geometrical refraction correction (神野有生, 2017), when the drone azimuth angles are 180-deg different, with (a) low overlap rate (b) high overlap rate, and (c) when the drone azimuth angles are equal.

Another geometrical correction method was presented by Murase et al., (2008). In this method, the depth correction is based on the two-view camera cases (stereo view) as shown in Figure 2-5 and Equation 2-6. In this method, the positions of two cameras (X_{S1} and X_{S2}), the position of apparent points (X_A), and the horizontal distance between the camera position and apparent points ($D_1$and D_2)

are required. Application of the procedure to coral reef bathymetry produced a corrected DEM with favourable accuracy (Murase et al., 2008). However, based on the result of the experiment conducted by Hsu and Wang. (2011), this method show the tendency to over-correct the DEM.

$$h = \frac{tan\, r_1.cos\, \theta_1 + tan\, r_2.cos\, \theta_2}{tan\, i_1.tan\, \theta_1 + tan\, i_2.cos\, \theta_2}\, h_A \qquad \text{Equation (2-6)}$$

Overall, in real underwater SfM-MVS photogrammetry, it is not feasible to correct the effect of refraction by using geometrical approach for some reasons: (1) the common SfM-MVS photogrammetry software does not output the information on which camera was used for estimating the coordinates of each point (in the dense point cloud), (2) the common photogrammetry software also doesn't give any information about how many images are used to estimate each 3D-point in the dense point cloud, and (3) the geometrical approaches for multi-view photogrammetry is more complex than the single/stereo cases, and no researcher has derived this approach.

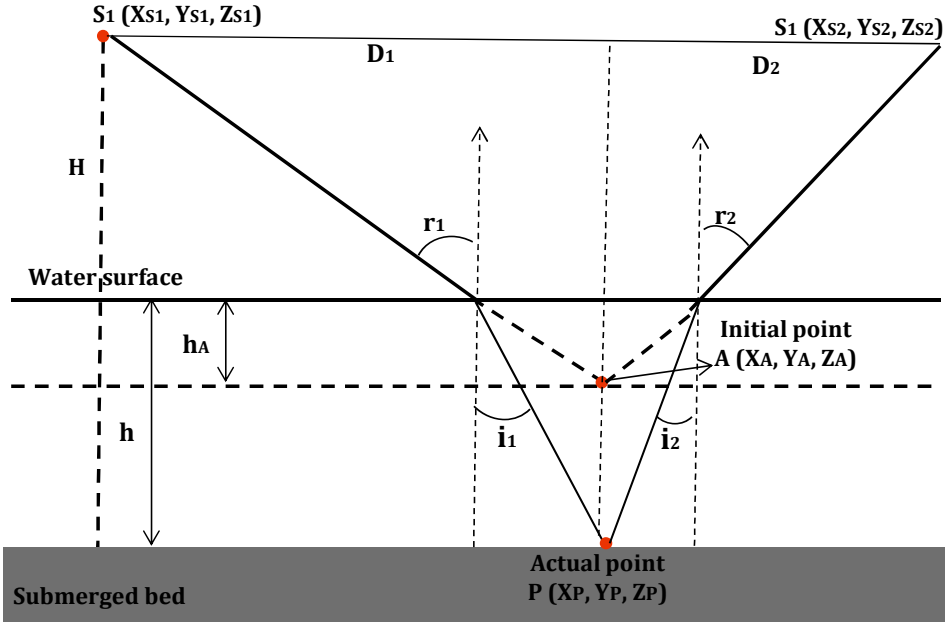

Figure 2-5. Geometry of two-medium photogrammetry (Murase et al., 2008).

B. Empirical linear correction method

One of evidence that the water surface refraction effect can be corrected by an empirical linear regression method is shown in the experiment proposed by 神野有生., (2018). In this experiment, they proposed the optimal correction factor on the basis of computer graphic-based simulation for various geometries. The simulation was done for each combination of altitude and overlap rate. The results of the experiment are shown in Table 2-1.

Table 2-1. Statistics of refraction correction factor (神野有生., 2018)

Height / water depth	Overlap ratio (%)		Statistics of Water surface refraction correction factor				
	X	Y	Mean	The first quartile (25 % value)	The third quartile (75% value)	standard deviation	The third quartile -the first quartile
30	70	90	1.4286	1.415	1.4489	0.01732	0.03384
	60	80	1.4234	1.3979	1.4498	0.02632	0.05188
	50	70	1.4274	1.4082	1.4448	0.02234	0.0366
	40	60	1.4123	1.3921	1.4385	0.03412	0.04639
	30	50	1.4113	1.3775	1.4429	0.0354	0.06543
60	70	90	1.4287	1.4149	1.4444	0.01834	0.02953
	60	80	1.4230	1.3980	1.4502	0.02757	0.05222
	50	70	1.4272	1.4083	1.4450	0.02367	0.03668
	40	60	1.4117	1.3901	1.4385	0.03499	0.04838
	30	50	1.4111	1.3779	1.4433	0.03638	0.06542
90	70	90	1.4284	1.4128	1.4416	0.01994	0.02874
	60	80	1.4237	1.3988	1.4500	0.02833	0.05121
	50	70	1.4256	1.4069	1.4436	0.02542	0.03665
	40	60	1.4100	1.3848	1.4393	0.03845	0.05455
	30	50	1.4104	1.3777	1.4422	0.03755	0.06453
120	70	90	1.4284	1.4109	1.4436	0.02231	0.03263
	60	80	1.4199	1.3930	1.4472	0.03122	0.05421
	50	70	1.4246	1.4049	1.4430	0.02721	0.03817
	40	60	1.4091	1.3837	1.4388	0.04056	0.05509
	30	50	1.4125	1.3777	1.4468	0.04195	0.06916

According to this table, the quartile widths (third quartile-first quartile) are very small (low variability of correction factor) when the overlap rates are high enough. This means, a single value of correction factor can be applied to correct the refraction effect of the whole model regardless of the altitude and the bottom texture. In other words, in high enough overlap rate, the linear regression method

which estimates the single value of CF and applies its value to calibrate the entire of survey areas is possible to correct the refraction effect of bathymetric measurement.

Hsu and Wang. (2011) developed a simple and empirical refraction correction method for close-range photogrammetry with multi-views stereo case. This correction method is based on the empirical relation between the real-scale apparent depths estimated by photogrammetry ($\widehat{h_A}$) and the real-scale measured true depth ($\widehat{h_R}$). In this method, the gain (β_1) and offset (β_0) of the linear regression formula is estimated by using least square method, as described below. The linear regression model has the form:

$$\widehat{h_R} = \beta_0 + \beta_1 \widehat{h_A} + e_i \qquad \text{Equation (2-7)}$$

where e_i is the residual.

The goal of the Least Square method is to find the estimated value p which minimizing the sum of the squares of the residuals (SSR), as shown below.

$$\text{Find min Q } (\beta_0, \beta_1), \quad \text{SSR} = \sum_{i=1}^{n} e_i^2 = \sum_{i=1}^{n} (\hat{h}_R - (\beta_0 + \beta_1 \hat{h}_A)^2 \qquad \text{Equation (2-8)}$$

The aim of this method is to find values for β_0 and β_1 such that SSR is minimized. In order to do this, the partial derivative of SSR with respect to each b_0 and b_1 are taken and equated to zero, *i.e.*

$$\frac{\partial SSR}{\partial \beta_0} = \sum_{i=1}^{n} 2(\hat{h}_R - (\beta_0 + \beta_1 \hat{h}_A)) = 0 \qquad \text{Equation (2-9)}$$

$$\frac{\partial SSR}{\partial \beta_1} = \sum_{i=1}^{n} 2(\hat{h}_R - (\beta_0 + \beta_1 \hat{h}_A))\hat{h}_A = 0, \qquad \text{Equation (2-10)}$$

The solution to these equations yields the least squares regression estimates:

$$\hat{\beta}_0 = \overline{h_R} - \hat{\beta}_1 \overline{h_A} \qquad \text{Equation (2-11)}$$

$$\hat{\beta}_1 = \frac{\sum_{i=1}^{n} (h_{Ri} - \overline{h_R})(h_{Ai} - \overline{h_A})}{\sum_{i=1}^{n} (h_{Ai} - \overline{h_A})^2}, \qquad \text{Equation (2-12)}$$

$$= \frac{Cov\ (\hat{h}_A, \hat{h}_R)}{Var\ (\hat{h}_A)}$$

$$= r_{\hat{h}_A \hat{h}_R} \frac{S_{\hat{h}_R}}{S_{\hat{h}_A}} \qquad \text{Equation (2-13)}$$

Where

- $\overline{h_R}$ and $\overline{h_A}$ denote the mean of $\hat{h}_R$ and $\hat{h}_A$, respectively;
- $r_{\hat{h}_A \hat{h}_R}$ denote the correlation coefficient between $\hat{h}_R$ and $\hat{h}_A$;
- $S_{\hat{h}_R}$ and $S_{\hat{h}_A}$ denote the uncorrected sample standard deviations of $\hat{h}_R$ and $\hat{h}_A$;
- Var and Cov denote the sample variance and sample covariance, respectively.

After the regression relation is constructed, it can be applied to derive the corrected water depth for the whole area of model. This method show better overall accuracy than the methods proposed by Butler et al., (2002) and Murase et al., (2008). In addition, this empirical linear regression method is not only corrects the effect of refraction, but also corrects for other effects, such as the systematic errors in DEM due to inaccurate estimation of camera extrinsic (position and orientation) and intrinsic parameters by SfM algorithm.

2.4.2 The existing of water surface reflection correction methods

Light arriving at the water surface can either be transmitted through the air-water interface or reflected from the surface, depending on the angle of incidence (Kay et al., 2009). The reflections effect occurs in an image when the sensor's view angle is equal to the angle of reflection of the direct solar beam. This effect often causes unusually bright pixel values in the imagery and obscures the water-leaving radiance signal of interest for mapping bathymetry (Overstreet and Legleiter, 2017). In SfM-photogrammetry, this effect caused the image matching fail in SfM process. This is because the image matching algorithm incapable to recognize conjugate (matching) points between overlapping images due to its inconsistency of brightness pixel value.

In some cases, the sun/sky reflections can be minimized through careful flight planning and image acquisition. The reflections intensity depends, among

other things, on illumination and viewing geometry, so flight paths can be designed to minimize water surface reflection effect. For framing cameras with a small field of view, collecting data when the sun is low in the sky implies that the sun reflection passes below the sensor field of view (Mount, 2005, Casella et al., 2016), and the reflection can be minimized, but data collection during these times often is avoided due to shadows from trees and banks in fluvial topographic assessment. Dietrich. (2016) suggested designing the flight plan by maximizing the noon sun at site of survey to reduce the reflections effect. In addition, this method could also minimize the shadows from the banks and over hanging vegetation. However, these methods cannot be applied in all atmospheric conditions (e.g., on overcast days), which limits the surveying time.

Dietrich. (2016) suggested another method to minimize the reflections effect by equipping the UAV's camera with a polarizing filter at image acquisition stage. This filter minimise the reflections by absorbing the light reflected from water surface, which is perpendicular to the direction of the filter. This filter is work best in sunny conditions, but not in cloudy days. In addition, the effect of polarizing filter in reducing the reflection effect is not uniform across the whole frame, as shown in Figure 2-6. The effect is maximal at an angle of 90 degree to the sun, and gradually tapers off on both sides of a frame. However, this technique is more practical compare to others existing methods as described above.

Westaway et al., (2001) presented a method to correct water surface reflection after photogrammetry process. In this method, the point clouds in which the photogrammetry was assumed to have not detected the bottom bed were manually eliminated. And then, the areas where point clouds had been eliminated were set to zero and re-interpolated the points to give the final corrected submerged bed elevation map. However, this method is time consuming and only be applied in the areas which contain very small reflections.

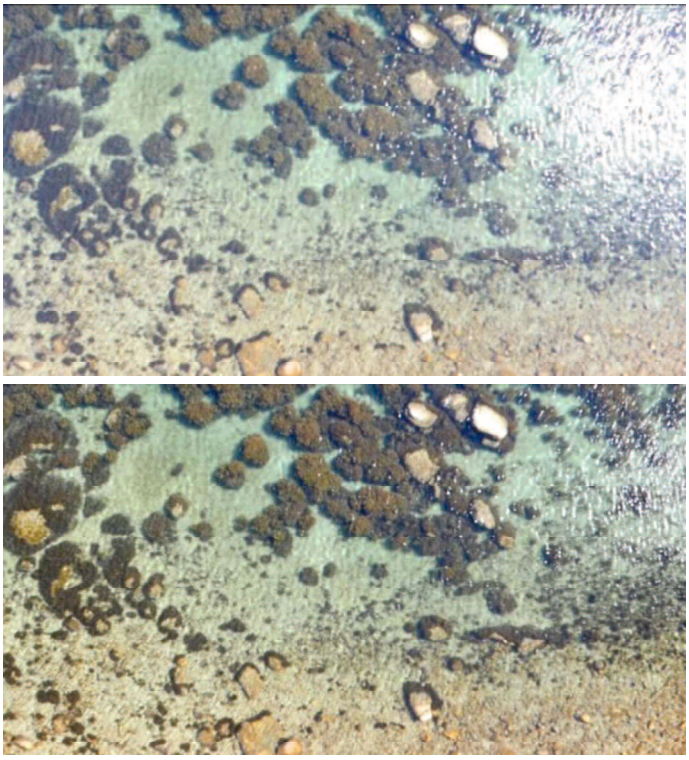

Figure 2-6. Images simulated without (a) and with (b) applying polarization filter.

Chapter 3. Development of Water-Surface Refraction Correction Technique for UAV-Based Photogrammetry of Shallow Water Bottom

3.1 Introduction

The accuracy and precision of DEM generated by UAV-based photogrammetry of shallow water bottom are slightly poorer in submerged areas, due to the refraction of light at the air-water interface. The submerged areas record shallower water depths than the reality due to this effect. Therefore, a refraction correction procedure is required.

In this study, an empirical approach that estimates a reasonable CF for a specific flight by minimizing the RMSE in the corrected bottom elevation was presented. The effectiveness of this approach was tested through its application to two river sites. The RMSE and ME values in the corrected bottom elevation were compared with those from three other existing methods: the no refraction correction approach (CF = 1), the conventional method using CF = 1.34, and a method using an empirical linear regression between measured and estimated water depth (Hsu and Wang, 2011).

3.2 Methods

3.2.1 Study site

In this study, the two test sites (Sites 1 and 2) were located at the main section of Saba River, Yamaguchi Prefecture, Japan. Site 1 is located about 8.5 km from Saba River Estuary, and Site 2 is located about 1.7 km upstream of Site 1. Figure 3-1 shows the extents of Site 1 and Site 2.

Table 3-1 lists the specification of each survey. The areas coverage at Site 1 and 2 were 51000 and 82000 m^2, respectively. During the UAV survey, the average

water depth was 0.6 m at Site 1 and 2. At site 1 and 2, the river bed was predominantly composed of gravel and sand.

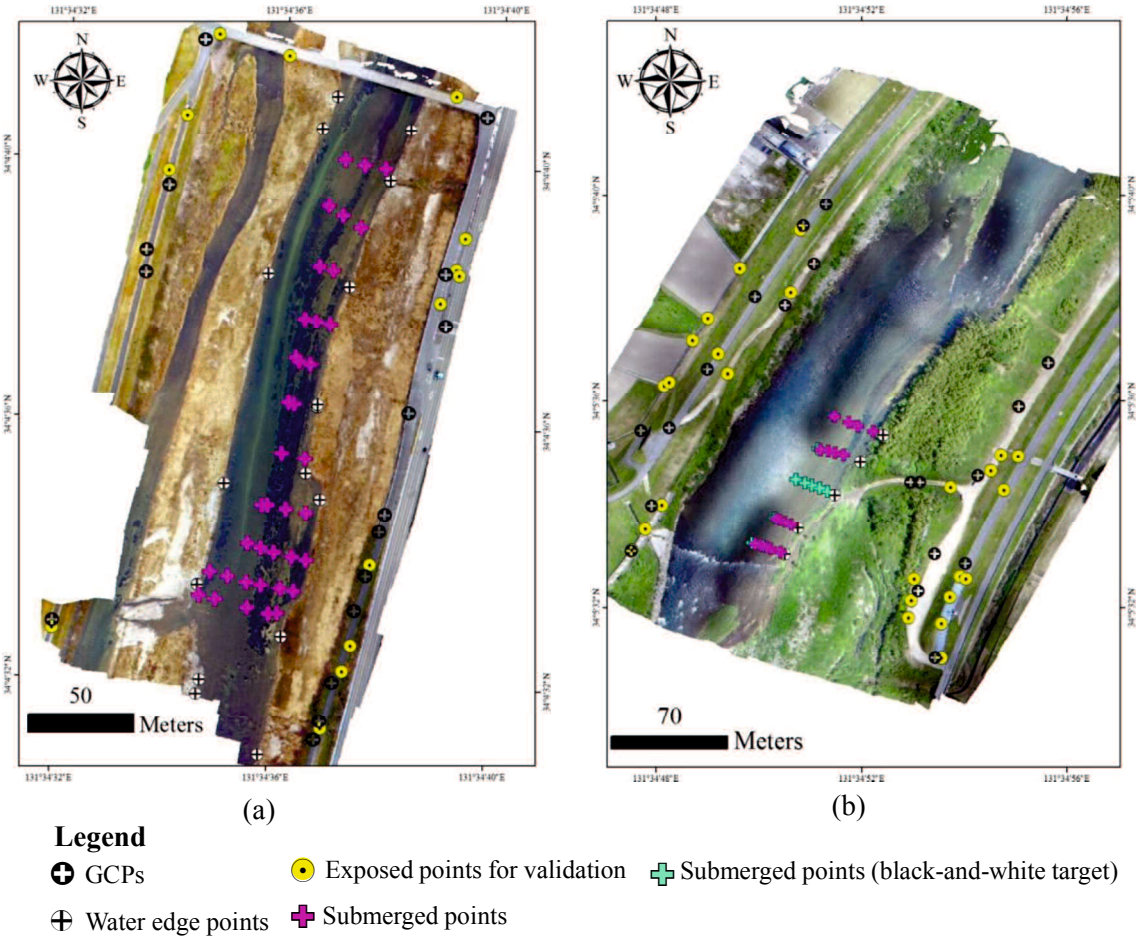

Figure 3-1. The study sites and spatial distribution of the points measured by RTK-GPS receiver in site 1 (a) and site 2 (b).

Table 3-1. Specifications of each survey.

Site location	**Site 1**	**Site 2**
Date of images acquisition	Jan 2016	May 2016
Time of day	3:47 PM – 4:15 PM	9:31 AM – 9:45 AM
Site dimension (m^2)	300 x 170	340 x 240
Depth range (m)	0 to ~ 1.5	0 to ~ 1.5

Bottom sediment characteristics	Cobble, gravel, and sand	Cobble, gravel, and sand
Visually observed wave height (m)	< 0.1	< 0.1
Wind speed (m/s)	2.5	5
Weather condition	Cloudy	Sunny

3.2.2 Image acquisition and image selection

Aerial photos were collected using a 4K digital camera attached to a small, lightweight (1.28 kg), quad-copter UAV (a DJI Phantom 3 Professional) (Figure 3-2). The UAV was flown at 25–30 m above ground level to give approximately 1 cm spatial resolution imagery of both sites. The resulting image footprint size was approximately 64 m × 48 m. Images were collected with a high level of overlap (> 80 %) to allow subsequent image matching during SfM processing. The total number of images collected at Sites 1 and 2 were 270 and 424, respectively. Figure 3-3 shows the samples of image taken using a stock camera on DJI Phantom 3 Pro at Site 1 and 2. During each field survey, the position of the camera was set to acquire imagery at the nadir (looking vertically downwards), to reduce the undesirable effects of reflection from the water surface on the acquired images. Finally, the images which contain the blurring effects were removed.

Figure 3-2. Unmanned aerial vehicle (UAV: DJI Phantom 3 Professional).

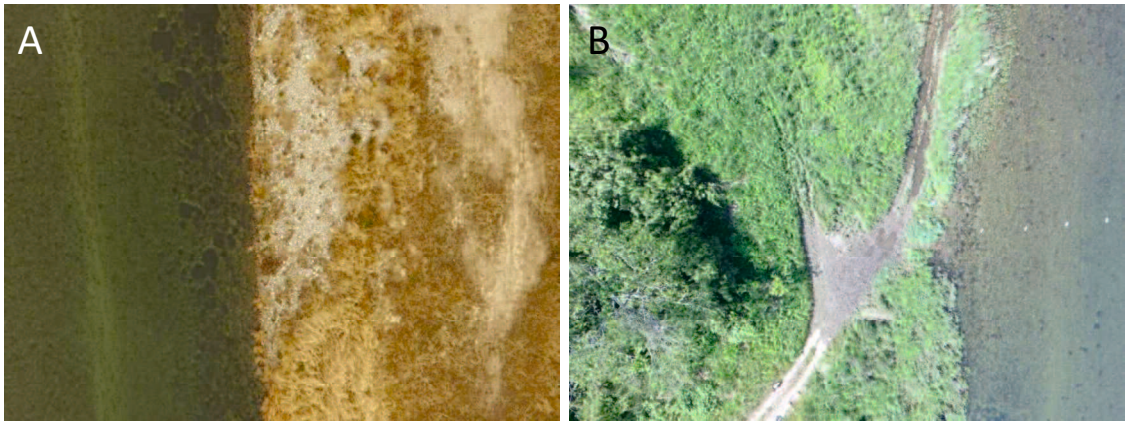

Figure 3-3. Example images acquired using a stock camera on DJI Phantom 3 Pro at (a) Site 1 and (b) Site 2.

3.2.3 RTK-GNSS measurements

The Real Time Kinematic-Global Positioning System (RTK-GPS receiver: Trimble R8s GNSS, Figure 3-4) measurements was performed at both exposed and submerged (underwater) points, as shown in Figure 3-1. Exposed points were landmarks recognizable in the aerial photos: stones, pins, and the black-and-white targets (Figure 3-5 (a)). They were distributed to cover the whole area as much as possible: on both banks of the river, and a bridge in Site 1. Some of them were used as Ground Control Points (GCPs) in the SfM-MVS procedure, and the others were used for validation of the SfM-MVS itself. In this experiment, the number of GCPs used at Site 1 and 2 were 16 and 19, respectively.

Submerged points were of two types. The first type includes the 10 black-and-white targets (Figure 3-5 (b)) only used in Site 2 (for validation of horizontal and vertical coordinates). The second were not marked and used as validation points (for validation of vertical coordinate) and were distributed to cover various depths and bottom types at Sites 1 and 2.

Figure 3-4. Real Time Kinematic-Global Positioning System (RTK-GPS receiver: Trimble R8s GNSS).

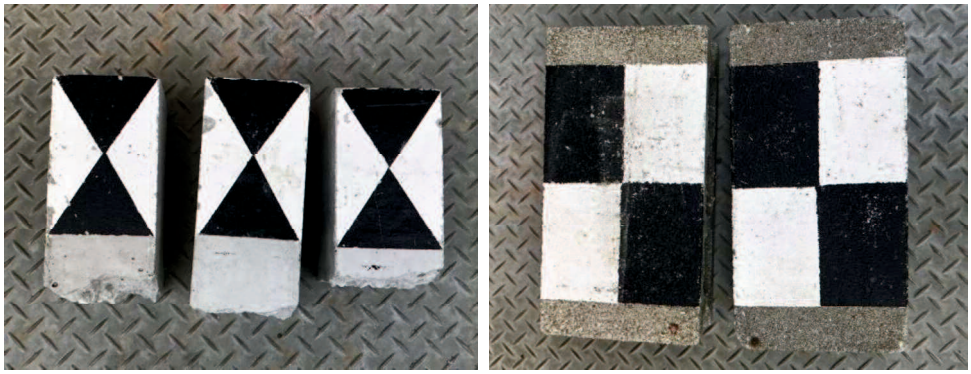

(a) (b)

Figure 3-5. Artificial ground control points (black-and-white target) constructed for (a) exposed area and (b) submerged area.

3.2.4 Generation of an apparent elevation map of the water bottom by SfM-MVS

The apparent elevation maps of the water bottom were generated at both sites using commercial software, Agisoft PhotoScan Professional version 1.2.6. First, SfM was performed to estimate the camera's extrinsic and intrinsic parameters, as well as the coordinates of the sparse point clouds. GCPs were used to give the world coordinates and to adjust some intrinsic parameters of the camera. Second, Multi-View Stereovision was performed to obtain the dense point clouds. Finally, the orthophoto and DSM were generated. The submerged area was

manually extracted for further analysis. The detail of SfM-MVS process was presented in Section 2-3.

3.2.5 Spatial interpolation of the water surface elevation

The estimated water surface elevation (WSE) model was constructed using a different method for each site. In Site 1, the WSE model was created by extracting water edge points from the orthophoto and DSM. The water edge points were extracted where the water's edge was clearly visible in the orthophoto. Thus, a two-dimensional linear interpolation technique was applied to build a two-dimensional model of the estimated WSE (Figure 3-6).

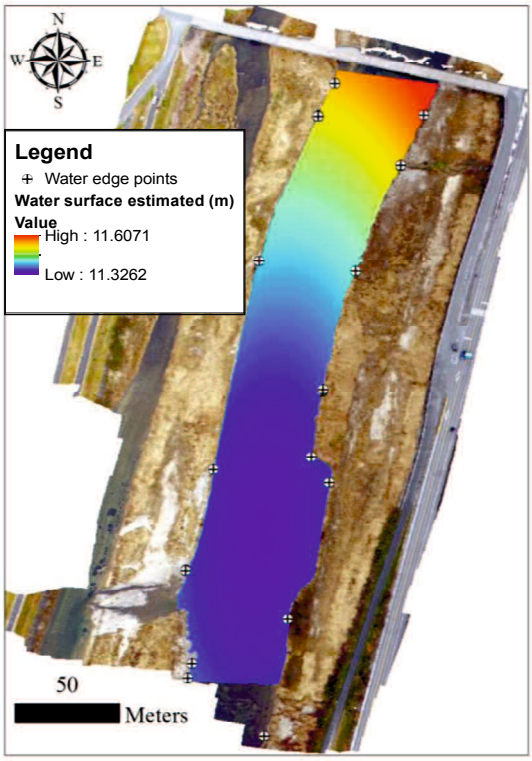

Figure 3-6. Example of water surface elevation map generated using a linear two-dimensional interpolation method at Site 1.

In Site 2, where the water's edge cannot be accurately detected visually using the orthophoto (due to overhanging vegetation), a conventional in situ technique with measurement devices (i.e. RTK-GPS receiver) was used to measure the water surface elevation at water edge points, and a one-dimensional linear

interpolation technique was applied to build a one-dimensional model of estimated WSE along the river channel. Figure 3-1 shows the distribution of measured water edge points at both sites.

3.2.6 Application of the general refraction correction methods

In this study, four refraction correction methods were tested to compare their performances. In fact, Method 1 corresponds to a no-correction case: the apparent elevation estimated by the SfM-MVS process is regarded as the refraction-corrected elevation. Methods 2 and 4 are the existing methods, and Method 3 is our proposed method.

In these methods, the refraction correction is based on the following equation:

$$h_R = p.h_A \qquad \text{Equation (3-1)}$$

where p is the gain of the refraction correction factor, h_R and h_A are the real-scale measured and apparent water depths estimated as

$$\hat{h}_R \equiv \hat{z}_{sfc} - z_{R,btm} \qquad \text{Equation (3-2)}$$

$$\hat{h}_A \equiv \hat{z}_{sfc} - \hat{z}_{A,btm} \qquad \text{Equation (3-3)}$$

Here, $\hat{z}_{sfc}$ is the water-surface elevation estimated by spatial interpolation of the elevations of water edge points (read from orthophotos or measured in situ), $z_{R,btm}$ is the real water bottom elevation measured by RTK-GNSS, and $\hat{z}_{A,btm}$ is the estimated apparent water bottom from SfM-MVS. If the biases (mean errors) is define in $\hat{h}_R$ and $\hat{h}_A$ as $\bar{\varepsilon}_R$ and $\bar{\varepsilon}_A$, Equation 3-1 can be rewritten as

$$\hat{h}_R = p.\hat{h}_A + \beta \qquad \text{Equation (3-4)}$$

where $\beta \equiv p.\bar{\varepsilon}_A - \bar{\varepsilon}_R$. Eq. (4) is the correction formula for water surface refraction.

Method 1 corresponds to using p=1 and β=0 in Equation 3-4. Method 2, proposed by (Westaway et al., 2001) and conventionally used by others (Woodget et al., 2015), uses p=1.34 and β=0, where the value 1.34 is the relative index of refraction for the air-water interface. In Method 4, proposed by (Hsu and Wang., 2011), p and β are estimated by linear regression (Least Square method) between $\hat{h}_R$ and $\hat{h}_A$. In Method 3, only p is estimated by linear regression (Least Square method) and β=0 is assumed.

3.2.7 Application of the proposed method

The overall workflow of the proposed method is summarized in this section. First, the apparent elevation map was generated by SfM-MVS method from UAV-imageries. Second, the elevations of water edge points were interpolated by using linear interpolation to generate the water surface elevation model. Third, the apparent elevation map was subtracted from the estimated water surface elevation model to generate the estimated apparent water depth map. The measured water depth points (h_R) were then compared with the pixel value of the estimated water depth (h_A) at the validation points by drawing the scatter gram of measured versus estimated water depth.

In this proposed method, the linear regression method (Least square method) with zero intercept was applied to estimate the correction factor (p). This linear regression method has the form:

$$\widehat{h_R} = p.\widehat{h_A} + e_i \qquad \text{Equation (3-5)}$$

where $\widehat{h_R}$, $\widehat{h_A}$ and e_i denote the measured value (measured real-scale water depth), estimated value (estimated real-scale apparent water depth), and residuals, respectively. The goal of the Least Square method is to find the estimated value p which minimizing the sum of the squares of the residuals (e_i), as shown below.

$$\text{Find min F } (p), \quad \text{for F } (p) = \sum_{i=1}^{n} e_i^2 = \sum_{i=1}^{n} (\hat{h}_R - p\hat{h}_A)^2 \qquad \text{Equation (3-6)}$$

The derivative of F should be 0:

$$\frac{\partial e_i^2}{\partial p} = 2\sum_{i=1}^{n}(\hat{h}_R - p\widehat{h_A})(\widehat{h_A}) = 0$$

$$p = \frac{\sum_{i=1}^{n}\hat{h}_A\hat{h}_R}{\sum_{i=1}^{n}\hat{h}_A^2} \qquad \text{Equation (3-7)}$$

Finally, the correction factor was multiplied with the estimated apparent elevation map to generate the estimated corrected water depth map. The workflow of the proposed method is summarized in Figure 3-7.

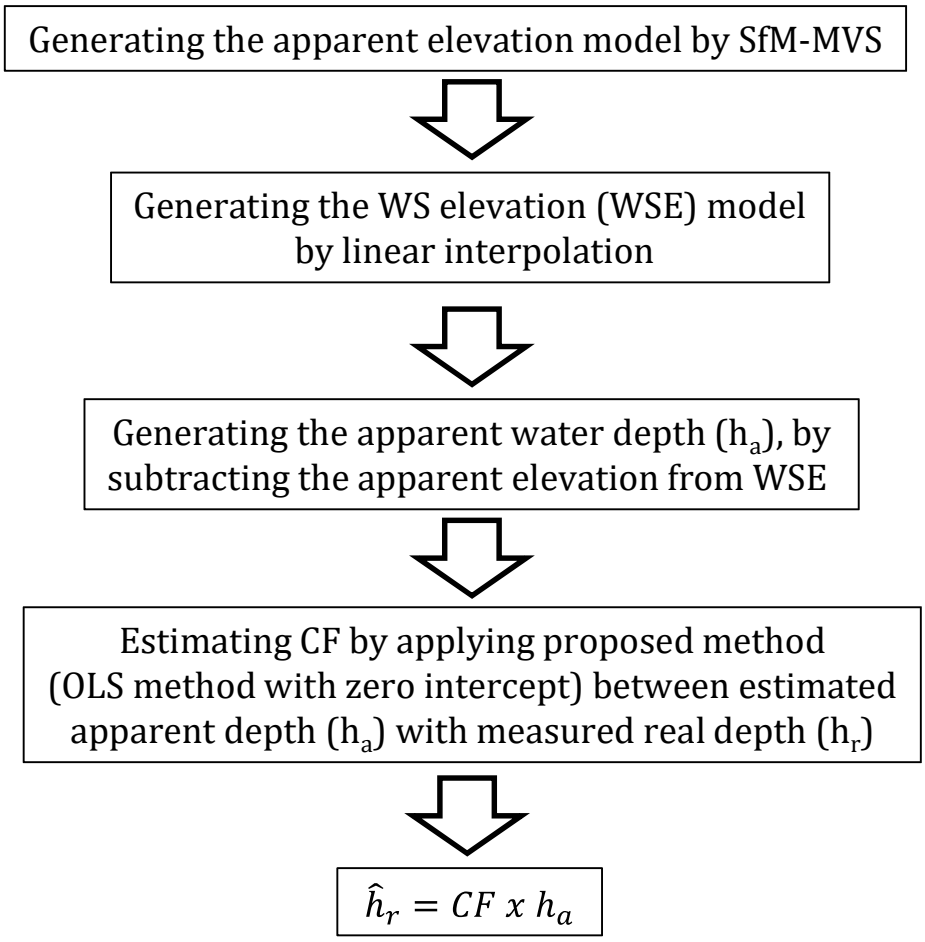

Figure 3-7. Workflow of the refraction correction by applying the proposed method.

3.2.8 Calculation of the refraction-corrected bottom elevation

To build the estimated refraction-corrected elevation map of the water bottom, a procedure from an existing method (Westaway et al., 2001) was followed (Figure 3-8). The first step of this method is generating the estimated apparent water depth map by subtracting the apparent elevation map of the water bottom from the water surface elevation map. Next, the apparent water depth map was multiplied by the empirical refraction CF to produce the refraction-corrected water depth map. Finally, to produce the refraction-corrected elevation map of the water bottom the refraction-corrected water depth map was subtracted from the estimated water surface elevation map.

3.2.9 Error evaluation and comparison

The RMSE and ME value was compared in the corrected bottom elevations from the four methods at each site. In order to evaluate the RMSE and ME for Methods 3 and 4, a cross validation was performed. The cross validation consisted of 1000 calibration/prediction trials. In each trial, the available underwater points with GPS measurements were randomly split into training and test data. The correction formula was calibrated for p and β (in Method 4) using the training data, and then used to predict the h_R of the test data. The RMSEs of the prediction errors for the 1000 trials were evaluated for each site and method. Because using many underwater GPS measurements for the calibration will not be desirable in practical applications, the cross validation for various numbers of training data was performed.

1. DATA ACQUISITION

UAV and GNSS Survey

a) Distribution & survey of GCPs using RTK-GPS
b) Collected independent topographic validation data using RTK-GPS
c) Image acquisition from UAV

2. DATA PROCESSING

UAV imagery

a) Manual image selection
b) SfM-MVS processing in Agisoft PhotoScan (see Figure X)
c) Export georeferenced orthophoto and DEM

3. ANALYSIS

Generation of corrected bottom elevation

a) Map positions of waters edge from orthophoto
b) Extract the water edge elevation points from DEM
c) Interpolate between elevation value using linear interpolation model to give estimated WSE
d) Subtract original DEM from estimated WSE to give estimated apparent depth
e) Estimated CF by linear regression between estimated apparent depth and measured true depth
f) Multiply estimated water depth by estimated CF to give refraction corrected real depth
g) Subtract corrected real depth from estimated WSE to give refraction corrected DEM in submerged areas

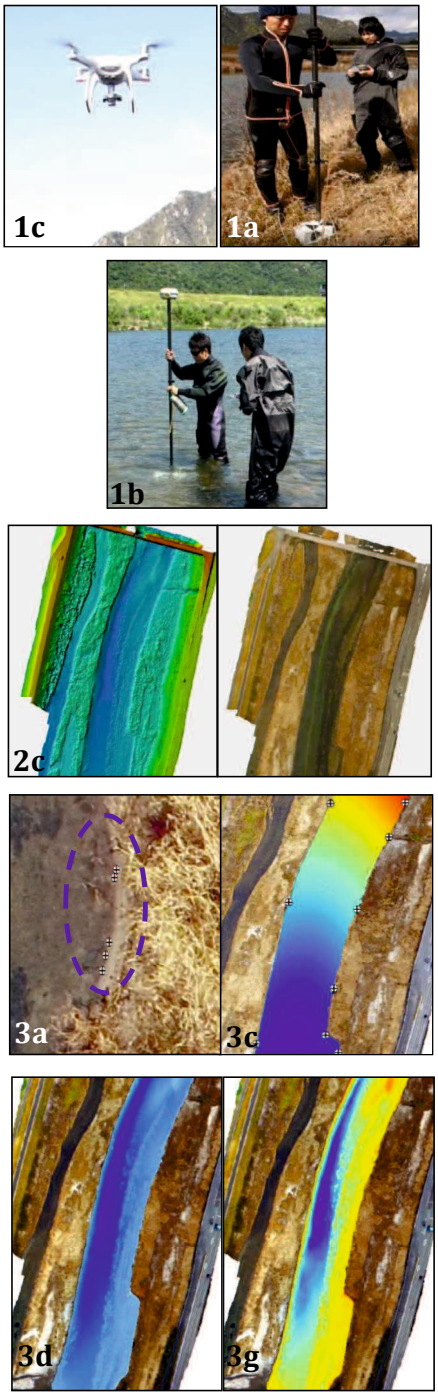

Figure 3-8. Workflow for generating the refraction-corrected shallow-water bathymetric map by using UAV-SfM photogrammetry.

3.3 Results and discussion

3.3.1 Validity of SfM-MVS in exposed areas

Figure 3-9 (a) shows the apparent elevation map generated by the usual SfM-MVS. Based on these figures, the river channel topography (from the embankment to the river bed) is possible to be observed in details. Table 3-2 lists the RMSE in the estimated X, Y, and Z coordinates of the GPS-measurement points not used as GCPs (Figure 3-1). For the exposed area, the RMSE for each axis was about 0.03 m on average for each site. It is of the same order as the general error in RTK-GPS measurements, and demonstrates the success of our SfM-MVS procedure.

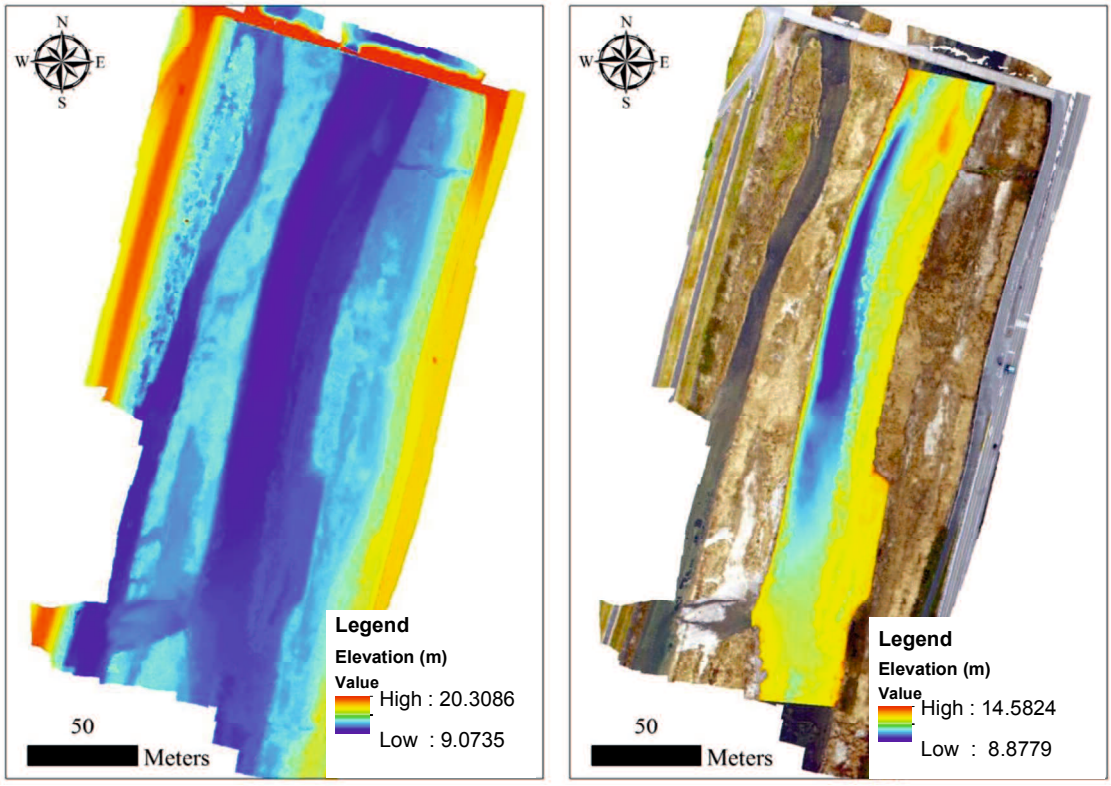

(a) (b)

Figure 3-9. Example of the resultant maps in Site 1. (a) the DEM generated by the SfM-MVS procedure (b) the refraction-corrected shallow water bottom elevation map by the proposed Method 3.

3.3.2 The necessity of refraction correction

Table 3-2 also lists the RMSE in the apparent bottom elevation obtained by the SfM-MVS procedure for 10 submerged black-and-white targets in Site 2. We can observe that the RMSE value for each of the X, Y, and Z coordinates is larger than that for the exposed area. Specifically, the RMSE values for the horizontal (X and Y) directions increased by a factor of only 1.6. On the other hand, in the vertical (Z) direction the RMSE increased by a factor of more than 3.4. In addition, the coefficient of determination in the vertical (Z) direction is smaller than the horizontal (X and Y) directions and the estimated Z coordinates tend to be overestimated, as shown in Figure 3-10 (c). This shows that the refraction effect increases the errors mainly in the vertical (Z) direction, and indicates the importance of the correction method in that direction, which is the topic of this paper.

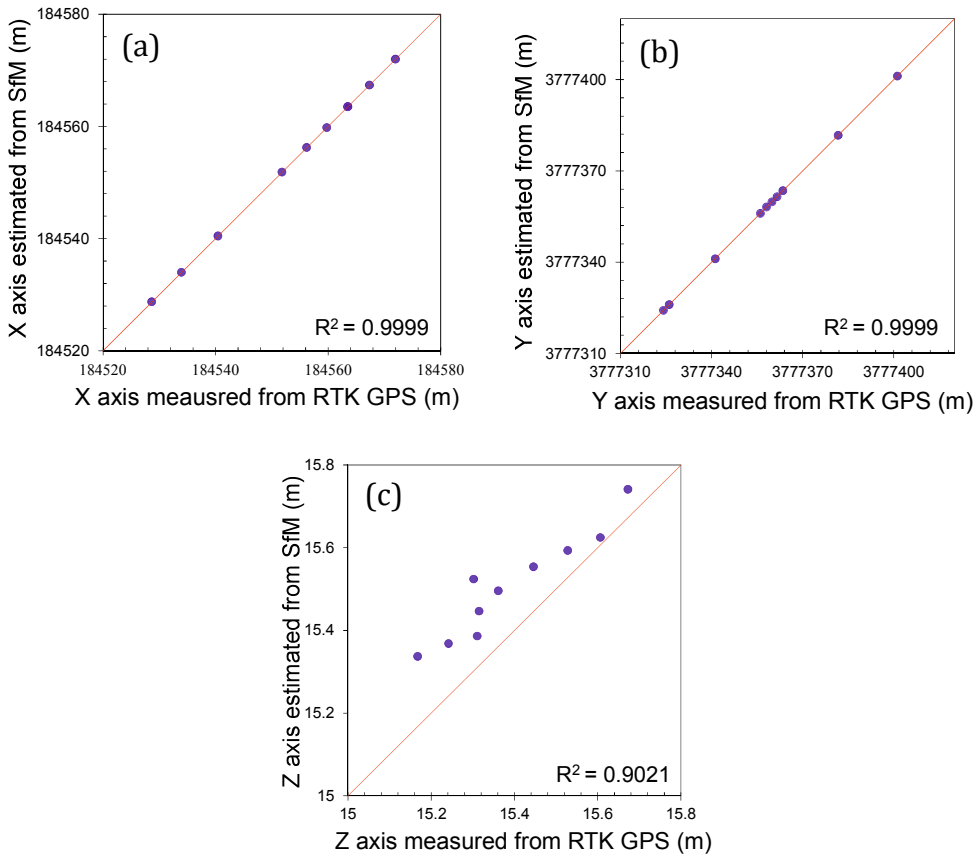

Figure 3-10. Elevation estimated from SfM-MVS, plotted against elevation measured from RTK-GPS at center of underwater markers for (a) X-axis, (b) Y-axis, and (c) Z-axis, in Site 2.

Table 3-2. Root mean square errors in the estimated X, Y, and Z coordinates of the GPS-measurement points not used as GCPs.

Site	Point type	RMSE (m)		
		X	Y	Z
1	exposed	0.0331	0.0192	0.0407
2	exposed	0.0306	0.0319	0.0371
2	submerged	0.0512	0.0505	0.1253

3.3.3 Error statistics for four refraction correction methods

Figure 3-9 (b) demonstrates the refraction-corrected shallow water bottom elevation map for Site 1 and Method 3. Figure 3-11 and Figure 3-12 show the RMSE and ME evaluated for each method at Sites 1 and 2, respectively. They were evaluated by the cross validation described above for Methods 3 and 4. For a visual understanding of the behaviour of each method, Figures 3-13 and 3-14 show the scatter plots of the corrected against measured bottom elevations for Sites 1 and 2.

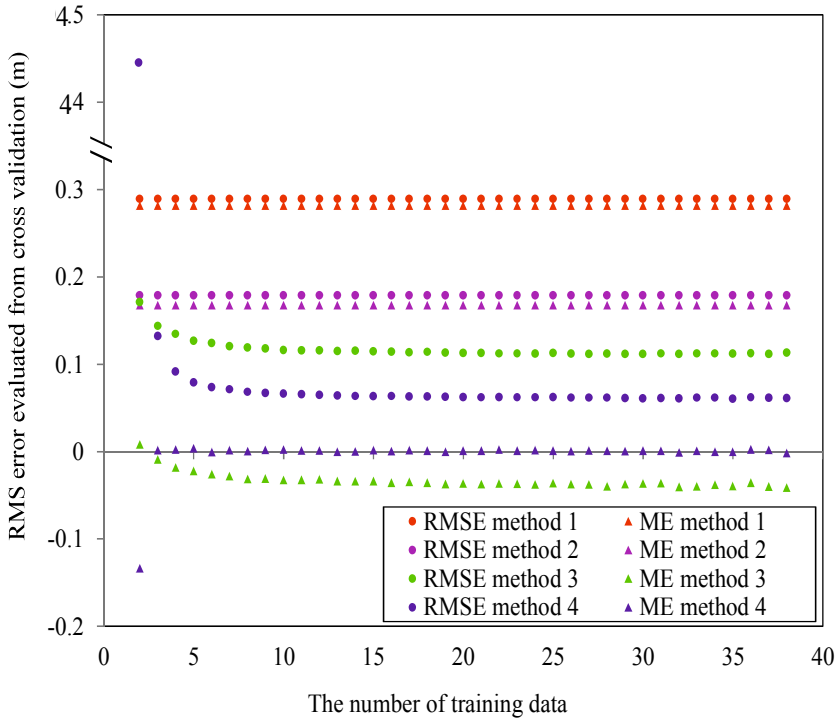

Figure 3-11. RMSE and ME evaluated for each method at site 1, by cross validation for Methods 3 and 4, for different numbers of training data.

Based on Figure 3-11 and Figure 3-12, overall, Method 1 resulted in the largest values of RMSE and ME (except for the case where Method 4 was calibrated with just two training data) due to the systematic overestimation (reflected in a large positive ME) introduced by neglecting the refraction effect. This result proves the necessity of a refraction correction.

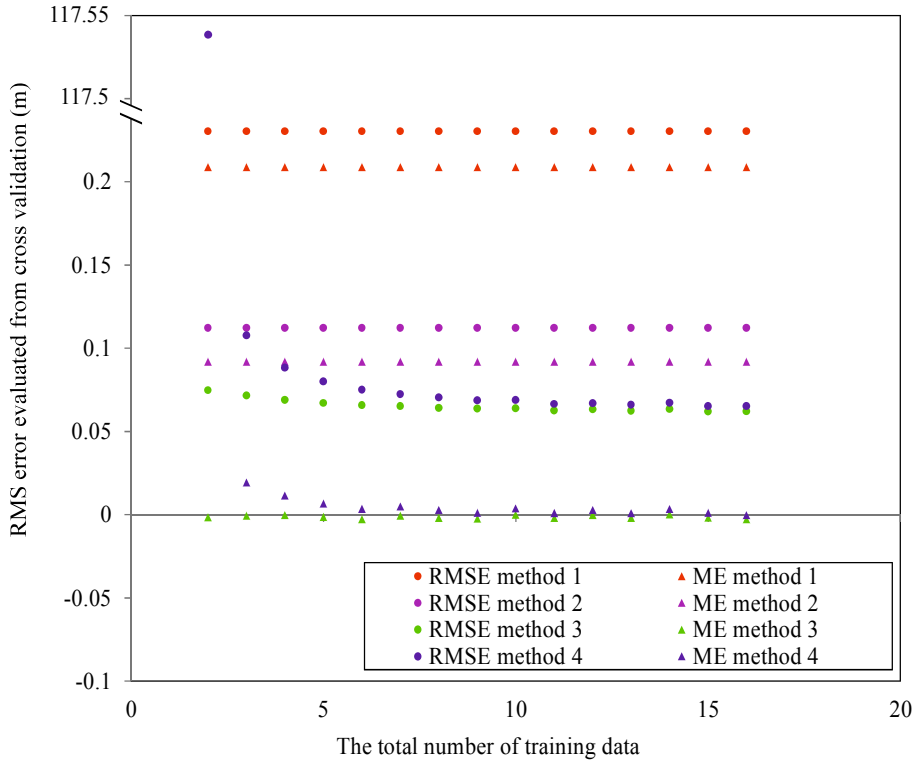

Figure 3-12. RMSE and ME evaluated for each method at site 2, by cross validation for Methods 3 and 4, for different numbers of training data.

As a result of the simple refraction correction, Method 2 resulted in RMSE and ME values about 40 % smaller than Method 1, but it still suffered from a significant systematic overestimation (i.e. a large positive ME). This demonstrates the geometrical fact, described in the Introduction, that a CF of 1.34 is the minimum possible value and is not enough in a real application.

Methods 3 and 4 outperformed Methods 1 and 2, except when the training data used for calibration were very few. For these methods, the RMSE and the ME increased as the number of training data decreased, and the increase was more

significant for Method 4. This is statistically natural: the more degrees of freedom a regression model has, the more unstable are the estimates of the coefficients, and the model requires more training data to function well. As a result, Method 4, which has two degrees of freedom in the correction formula, yielded extremely large errors when the number of training data was two (the minimum possible number). On the other hand, Method 4 gave smaller magnitudes of RMSE and ME than Method 3 in Site 1 when the number of the training data was three or more.

Excluding the case where the training data numbered only two, Method 4 was superior (in terms of RMSE) in Site 1, and Method 3 was superior in Site 2, regardless of the number of training data (Figure 3-11 and 3-12). ME also showed a similar tendency. Therefore, we need to conclude that the best method depends not only on the number of training data but also on many other factors. Because the two methods are different only in the existence of the intercept (β) in Eq. (4), the best method depends on the true magnitude of β. As β depends on the errors in estimating the apparent elevations of the water surface and bottom, the best method may change depending on the site, image acquisition conditions, GPS measurement conditions, and so on. In Site 1, the offset is large because the WSE was extracted from orthophoto and DSM. On the other hand, In Site 2, the offset is very small (close to zero) because the WSE was measured by RTK-GNSS. Overall, we conclude that Method 3 is superior of any other methods when the WSE was measured by RTK-GNSS.

Because it is impossible to know the true value of β, we propose statistically selecting the best method in each situation. One recommended selection method is the leave-one-out cross-validation, a cross-validation that uses only 1 test datum in each trial, and thereby can simulate the prediction errors when all the available GPS measurements are used for the calibration.

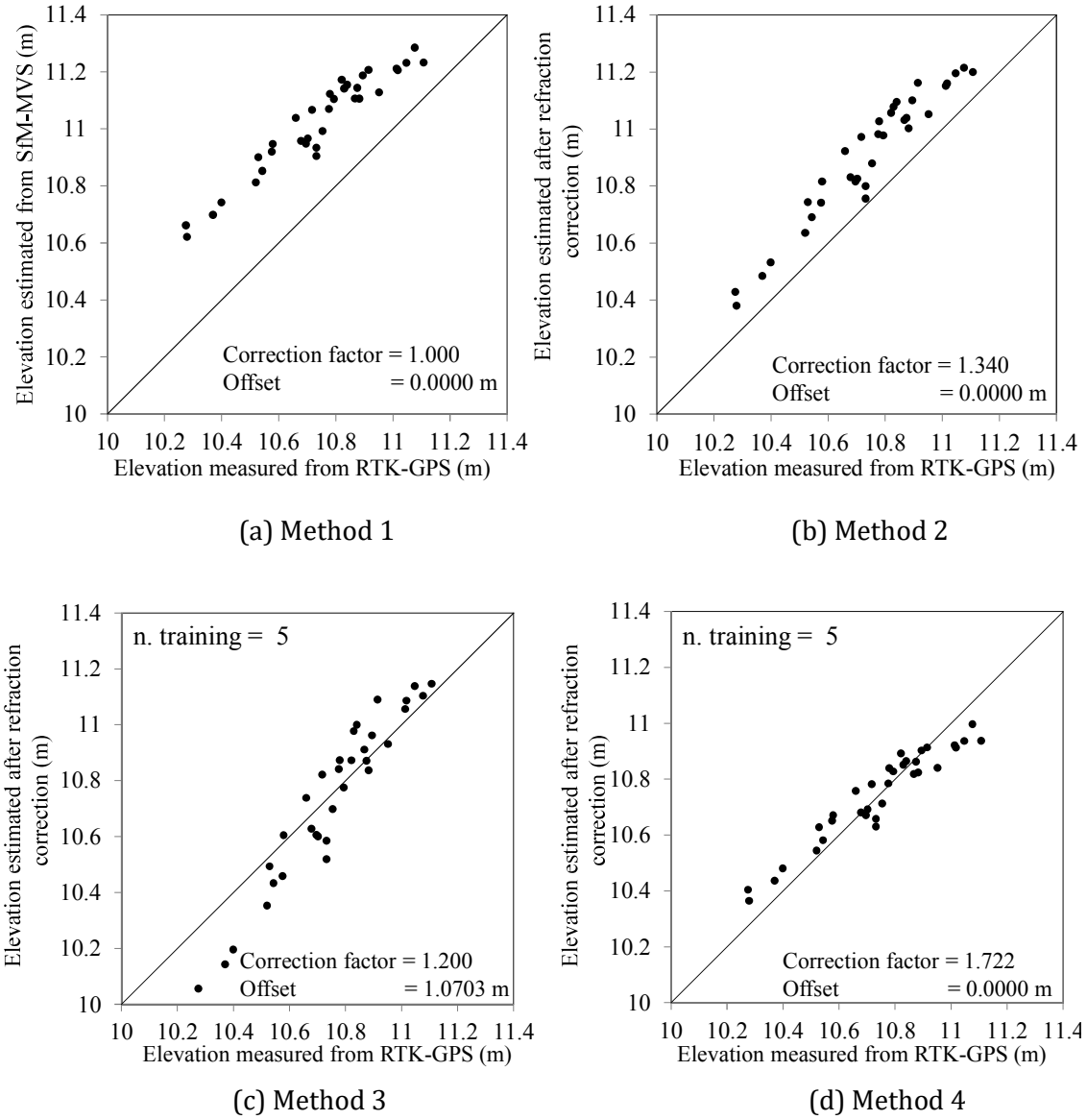

Figure 3-13. Elevation estimated after correction, plotted against elevation measured from RTK-GPS receiver, in Site 1 for (a) Method 1, (b) Method 2, (c) Method 3, (d) Method 4. For Methods 3 and 4, the figure shows the goodness of fit rather than prediction performance because all the plotted data were used to calibrate these methods.

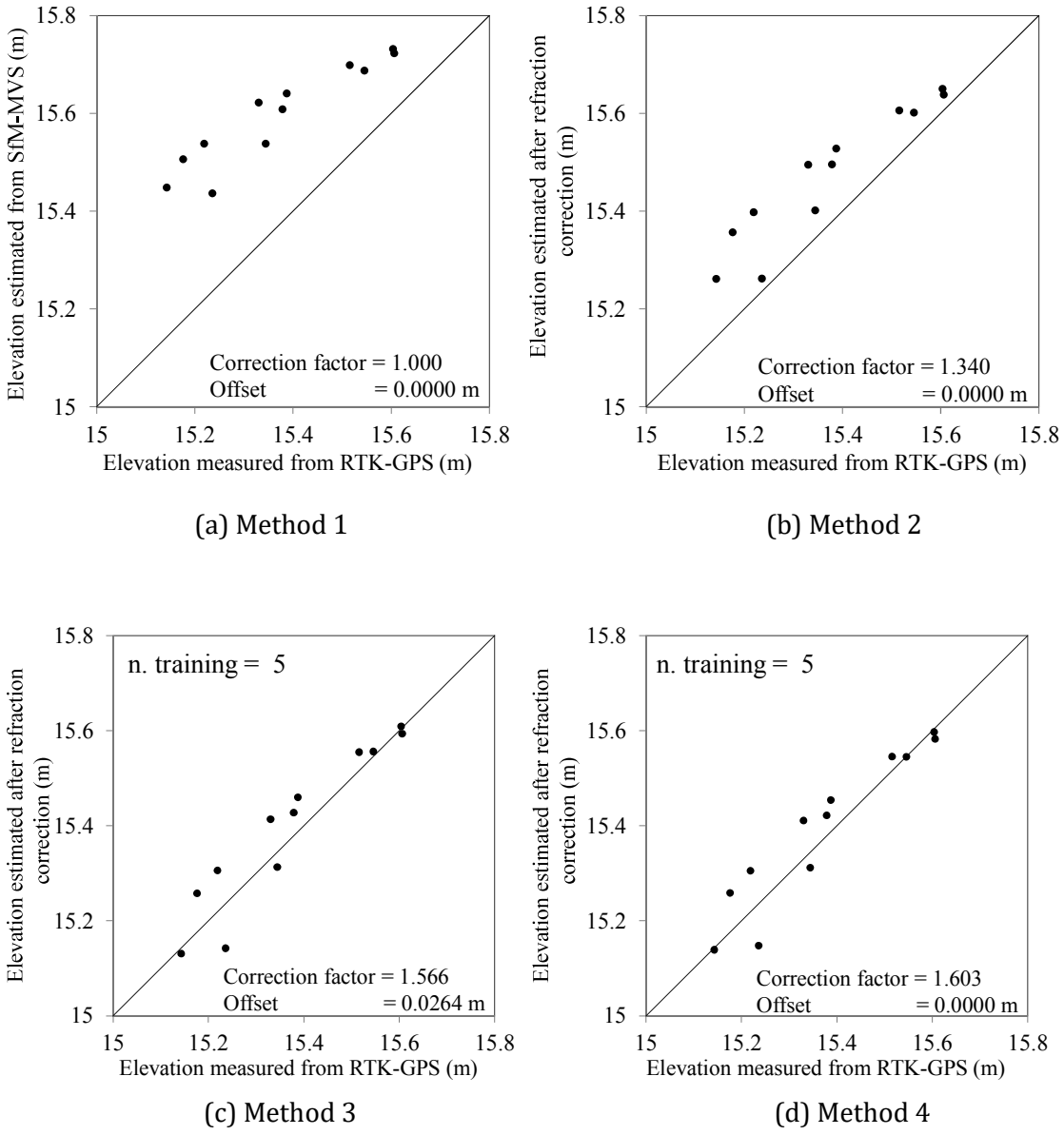

Figure 3-14. Elevation estimated after correction, plotted against elevation measured from RTK-GPS receiver, in Site 2 for (a) Method 1, (b) Method 2, (c) Method 3, (d) Method 4. For Methods 3 and 4, the figure shows the goodness of fit rather than prediction performance because all the plotted data were used to calibrate these methods.

3.3.4 Unrealistically small correction factor in Site 1

The proposed method (Method 3) produced realistic correction factor values in both Site 1 and Site 2, as listed in Table 3-3. On the other hand, the correction coefficient produced by Method 4 was unrealistically small in Site 1.

This might be due to the large noise contained in h_A. This is likely because in Site 1 the water surface elevations at the water edges were read from the orthophoto, and thus contain errors resulting from unclear edge readings as well as the photogrammetry itself.

In order to examine this hypothesis, another numerical experiment was performed to observe the effect of the noise in h_A on the estimated correction factor. In this experiment, the artificial normal noise with zero mean and various standard deviations was added to h_A, and then the correction factor was estimated, and observed how it changes in response to the noise levels. Such estimation was done 1000 times for each method and for each site, using a same seed of random number generator. The result is summarized in Figure 3-15.

Table 3- 3. Correction coefficients for each method and site. For methods 3 and 4, the coefficients were calculated using all the available underwater GPS measurements.

Method	Correction Factor p		Offset β (m)	
	Site 1	Site 2	Site 1	Site 2
1 (no correction)	1.000		0.0000	
2 (conventional)	1.340		0.0000	
3 (proposed)	1.722	1.603	0.0000	0.0000
4 (linear regression)	1.200	1.566	1.0703	0.0264

For Method 4, the mean of the estimated correction factor significantly decreases as the noise level increases, supporting the hypothesis described above. This means that Method 4 suffers from a large negative bias in the correction factor when h_A is noisy. This is a statistical fact in linear regression method. Based on Equation 2-13, if the noise level contained in h_A increases, the standard deviation of h_A ($S_{\hat{h}_A}$) increases and the coefficient of correlation ($r_{\hat{h}_A \hat{h}_R}$) decrease, this causes the gain (β_1) value significantly decreases and tends to close to zero. Figure 3-16 demonstrated this fact.

On the other hand, the decrease for Method 3 is much less, showing the robustness of Method 3 against noise in h_A. This result indicates the superiority of Method 3 in terms of the geometric soundness of the estimated correction factor.

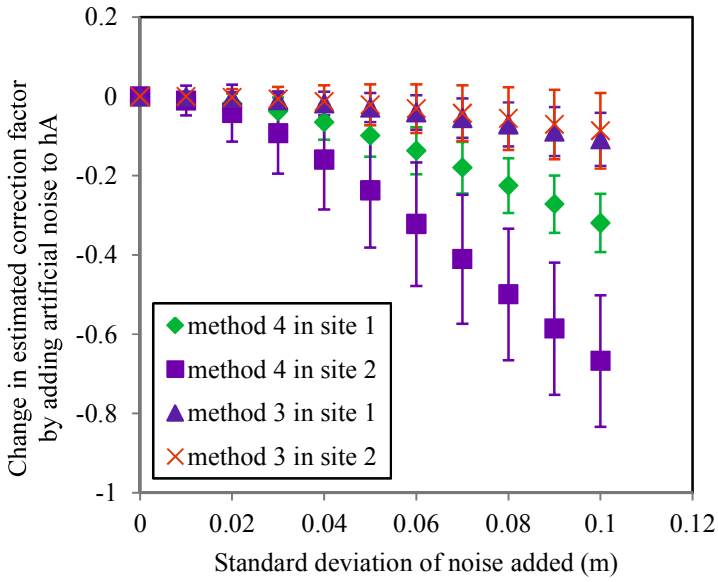

Figure 3-15. The change in estimated correction factor when artificial normal noises were added to h_A. Points show the mean values, and error bars show the standard deviations, in 1000 trials.

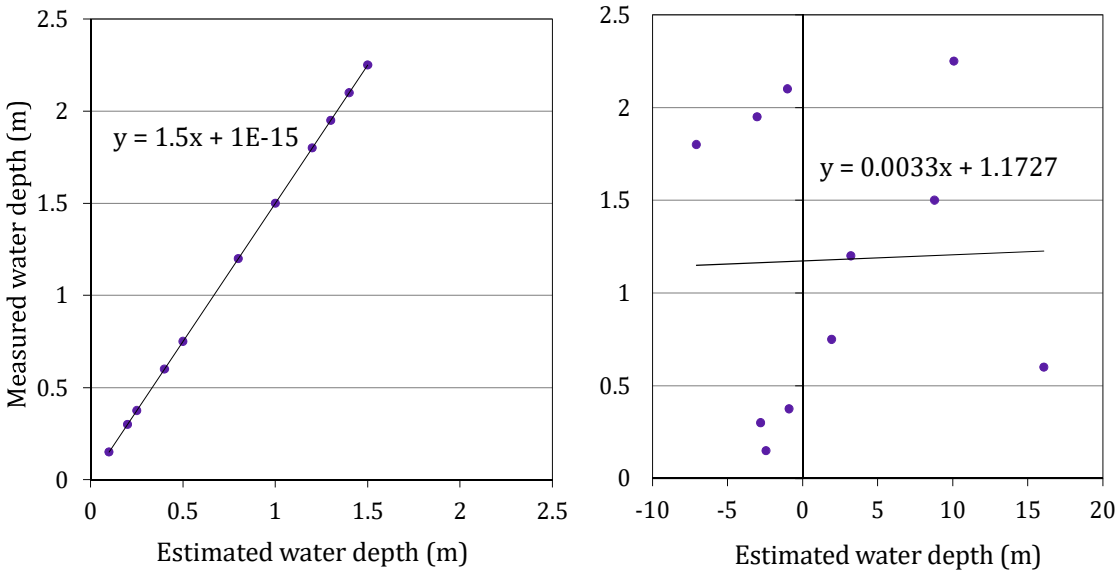

(a) No error case (b) Very large noise case

Figure 3-16. Scatter plots of the measured against estimated water depth, (a) without noise case and (b) very large noise case in h_A.

3.4 Summary and conclusion

This study presented and examined a new empirical method to correct for the effect of refraction after the usual SfM-MVS procedure using common software. The presented method converts the apparent water depth into a refraction-corrected (real-scale) water depth by multiplying by an empirical correction factor. The effectiveness of this method was examined by applying the method to two river sites, and comparing the RMS and mean errors in the corrected bottom elevation with three existing approaches. Overall, the presented method outperformed two of the existing methods: the no-correction approach (Method 1) and the method using the relative index of refraction (1.34) as the correction factor (Method 2). The presented method is superior of any other methods in Site 2. Even in Site 1, the presented method was better than Method 4 when the number of training data is few and the WSE was measured by RTK-GNSS. The remaining existing method (Method 4), which adds an empirical offset after multiplying by the empirical correction factor, was unstable when the training data for calibration were very few. In addition, we found that the linear regression method (Method 4) suffers from a large negative bias in the correction factor when the apparent water depth estimated is noisy. We conclude that the most accurate correction method in terms of the bottom elevation depends on many factors (e.g. site, image acquisition conditions, GPS measurement conditions), and should be statistically selected, for example by leave-one-out cross validation.

Chapter 4. Development of Water-Surface Reflection Removal for UAV-Based Photogrammetry of Shallow Water Bottom

4.1 Introduction

The applicability of UAV-based shallow-water photogrammetry technique is sometimes limited by sun and sky reflection at the water surface. As mentioned in some studies (Dietrich, 2016, Casella et al., 2016), these reflections hinder the matching between images in some cases, rendering the point-cloud density and accuracy insufficient. Therefore, a technique to reduce the water-surface reflection effect is required.

In the present study, a new imaging technique was presented to suppress the effect of water-surface reflection. In this technique, the drone was ordered to take a short video at each waypoint; and then apply a temporal minimum filter (TMF) to this video. The filter extracts the smallest RGB values in all the video frames for each pixel, and composes an image with small reflection effects. To assess the performance of this technique, the method was applied at three shallow-water sites, and evaluated its effect on the point cloud density and the accuracy and precision of the photogrammetry, in comparison with the case of a randomly chosen frame.

4.2 Methods

4.2.1 Study site

Sites 1 and 2 were located in a coastal area of the Seto Inland Sea, Yamaguchi Prefecture, Japan. Although these locations were almost identical, I defined them as two separate sites because the main target area (the internal area to be shot from 40 or more camera positions in accordance with the research plan), the number and distribution of the GCPs, and the validation points were different. Moreover, the two sites were surveyed on different dates (Table 4-1). Site 3 was

located on the main section of the Saba River, in Yamaguchi Prefecture. Figure 4-1 shows the extents of Sites 1, 2, and 3, overlaid with orthophotos.

Table 4-1 lists the specifications of each survey. The areas of the main targets at Sites 1, 2, and 3 were 400, 400, and 1200 m^2, respectively. During the UAV survey, the average water depths were 1.0, 0.6, and 0.7 m at Sites 1, 2, and 3, respectively. At Sites 1 and 2, the bed was predominantly composed of rock and cobble, while that at Site 3 was predominantly composed of gravel and sand. Although I did not quantitatively measure the water clarity, I could recognize the bottom texture in the UAV-based pictures even at the deepest validation point (2.2, 1.5, and 1.3 m for Sites 1, 2, and 3, respectively) at each site.

Table 4-1. Specifications of each survey.

Site location	**Site 1**	**Site 2**	**Site 3**
Date of data acquisition	Jan 2017	Dec 2016	Jan 2017
Time of day	11:30 AM–3:30 PM	09:30 AM–12:30 PM	11:00 AM–2:30 PM
Spatial coverage area (m^2)	4400	3400	7000
Site dimension (m^2)	80 x 60	90 x 40	90 x 80
Main target areas as percentage of total coverage	9	12	18
Depth range in main target area (m)	0 to ~2.5	0 to ~2.5	0 to ~1.5
Bottom sediment characteristics	Rock, cobble, gravel, and sand	Rock, cobble, gravel, and sand	Cobble, gravel, and sand
Visually observed wave height (m)	< 0.1	< 0.1	< 0.1
Wind speed (m/s)	1 to 3.5	1.5 to 4.5	3 to 6
Weather condition	Sunny	Cloudy	Cloudy

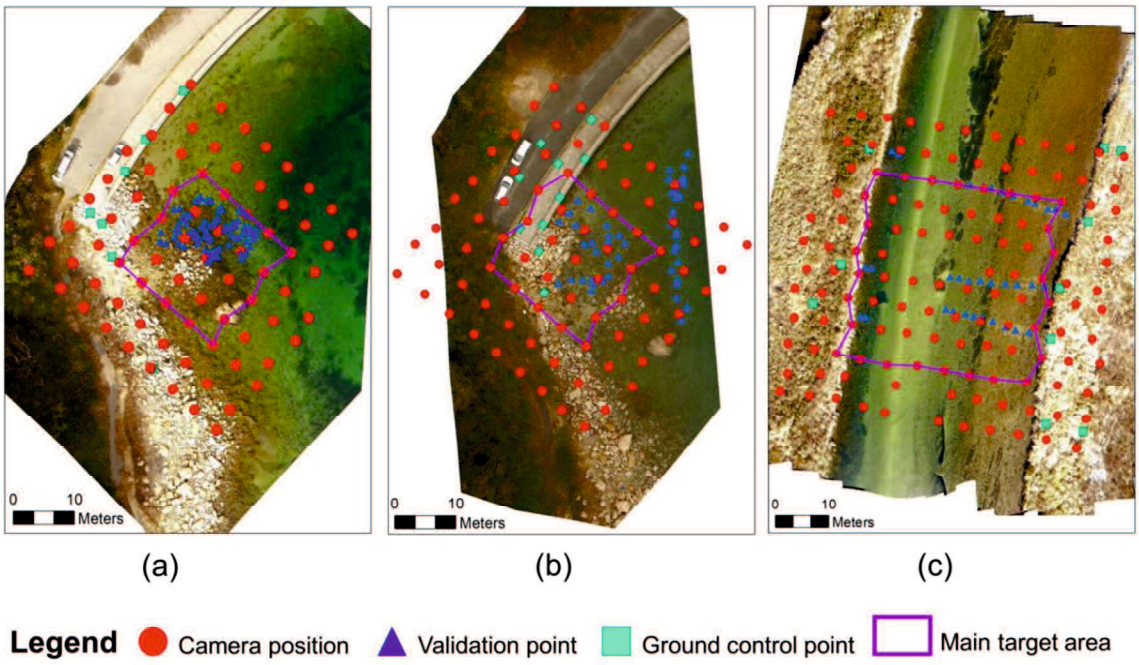

Figure 4-1. Distribution of drone waypoints, ground control points, and validation points at Sites (a) 1, (b) 2, and (c) 3, overlaid with orthophotos generated for each site. At each validation point, world coordinates were measured by total station theodolite (TST) or real-time kinematic global positioning system (RTK-GPS receiver). The orthophoto shown for each site includes the surrounding area of the main target area (the area to be shot from 40 or more camera positions), to provide a clear overview of the environment.

4.2.2 Video collection

Video recordings were collected using a stock camera (4K/ultra-high-definition camera; angle of view: 94 degrees; resolution: 3840 × 2160 pixels; frame rate: 29.97 frames/s; color depth: 24 bit in YUV color space) on a small, lightweight (1.38 kg), quad-copter UAV (a DJI Phantom 4) (Figure 4-2). The camera was set to point directly downward (nadir), because this is the most basic and widely used setup, even though some studies suggest that off-nadir imagery is preferable for SfM (James and Robson, 2014, Carbonneau and Dietrich 2017). The UAV was flown 30 m above ground level (at the drone's home point), which yielded a ground resolution of 0.01 m. The UAV waypoints were arranged in a 9 × 9 lattice pattern of 81 points at both Sites 1 and 2, and a 12 × 12 lattice pattern of 144 points at Site 3,

with spacing between waypoints of 5 m. At each waypoint, 3 s of video (90 video frames) were recorded.

Figure 4-2. Unmanned Aerial Vehicle (UAV: DJI Phantom 4).

4.2.3 Ground control points and validation points

The GNSS (Global Navigation Satellite System) measurement was performed using the Real Time Kinematic-Global Positioning System (RTK-GPS receiver: Trimble R8s GNSS, Figure 3-4) at Site 3 and conducted Total Station Theodolite (TST: SOKKIA SET530RS, Figure 4-3) measurement at Sites 1 and 2, at both exposed and submerged (underwater) points, as shown in Figure 4-1. Exposed points were used as GCPs in the SfM–MVS procedure.

Figure 4-3. Total Station Theodolite (TST: SOKKIA SET530RS).

These points were defined at the centers of the circular black-and-white markers with diameters of 0.2 m, and a quadrant pattern was painted (Figure 4-4). In this experiment, 7 GCPs were used at Site 1 and 10 each were employed at Sites 2 and 3. Submerged points were not marked and used as “validation points”, and were set at various depths.

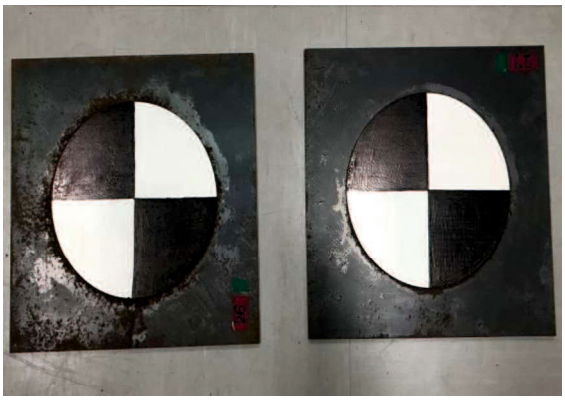

Figure 4-4. Artificial black-and-white marker used as GCP in the field survey.

4.2.4 Generation of Input Images

As the first step in processing, the effects of the displacement and rotation of the camera, caused by the movement of the UAV during the recording were removed. This was achieved using the “Warp Stabilizer VFX” tool in Adobe After Effects CC 2017. First, this tool creates track points on static objects in each frame of a video. Second, the tool matches track points between frames and calculates the tracking data, i.e., the translation, rotation, and scale change between track points. Then, the tracking data are used to generate a video without motion effects, which has the appearance of being taken from one static position with no horizontal rotation during recording. After this process, the near-edge region that was not visible in all frames was cropped. Finally, the frames of each resultant video were exported in PNG (Portable Network Graphics) sequence format with 24-bit depth color in RGB color space for further analysis.

To confirm the effectiveness of the motion removal, the magnitude of motion of two static points (center points of two black-and-white targets) in the

videos before and after stabilization were evaluated. First, the u and v pixel coordinates (the number of pixels from the left and top of the image, respectively) of each point in each of the 90 frames of each video were manually measured. Then, the standard deviations of the u and v coordinates for each point and video were evaluated. Hence, I confirmed that the standard deviations, originally more than four pixels, were reduced to subpixel level by the motion removal (Table 4-2).

From the resultant videos, a subset (2 s of video: 60 video frames) at each waypoint was selected to generate the input images for the SfM-MVS procedure. There are two main reasons for selection of 2 s of video. First, for efficiency in practice, the recording time should not be excessively long. Second, the periods of steep-slope waves (including capillary waves) are usually less than 2 s.

Table 4- 2. Standard deviations of *u* and *v* pixel coordinates of two static points in videos before and after stabilization.

Stabilization	Standard deviation of pixel coordinates (pixel)			
	Point 1		Point 2	
	u	*v*	*u*	*v*
Before	5.475	9.791	4.455	6.444
After	0.789	0.377	0.459	0.429

Two sets of input images were generated from the resultant video for the SfM–MVS procedure. One set was generated by applying a temporal minimum filter to the 60 frames of video from each waypoint, in order to reduce the effect of water surface reflection. The other set of images was generated by randomly selecting one frame from the 60 frames at each waypoint, in order to simulate an image obtained by normal photography. Hereafter I call usage of the first set as the "proposed technique" and usage of the second set as the "normal technique." I note that the normal technique does not fully simulate normal photography well, because video frames are usually degraded by various artefacts due to

encoding/decoding and have lower resolutions than still photographs. Nevertheless, I chose to "simulate" the normal photography in this way rather than to take "real" photographs, in order to unify the image resolution and environmental conditions (e.g., light and capillary wave fields) between the two cases.

Figure 4-5 illustrates the idea of the TMF. Each pixel is given the darkest value (the lowest brightness intensity, when the light reflected from the surface is expected to be minimal) from the set of 60 images at that waypoint. This filter was applied for each of the R (Red), G (Green), and B (Blue) components of 24-bit color. In other words, the processing picks up the smallest RGB values for each pixel from all 60 frames in order to generate an image with low-intensity water surface reflection. Figure 4-6 presents images obtained using both the proposed and normal techniques.

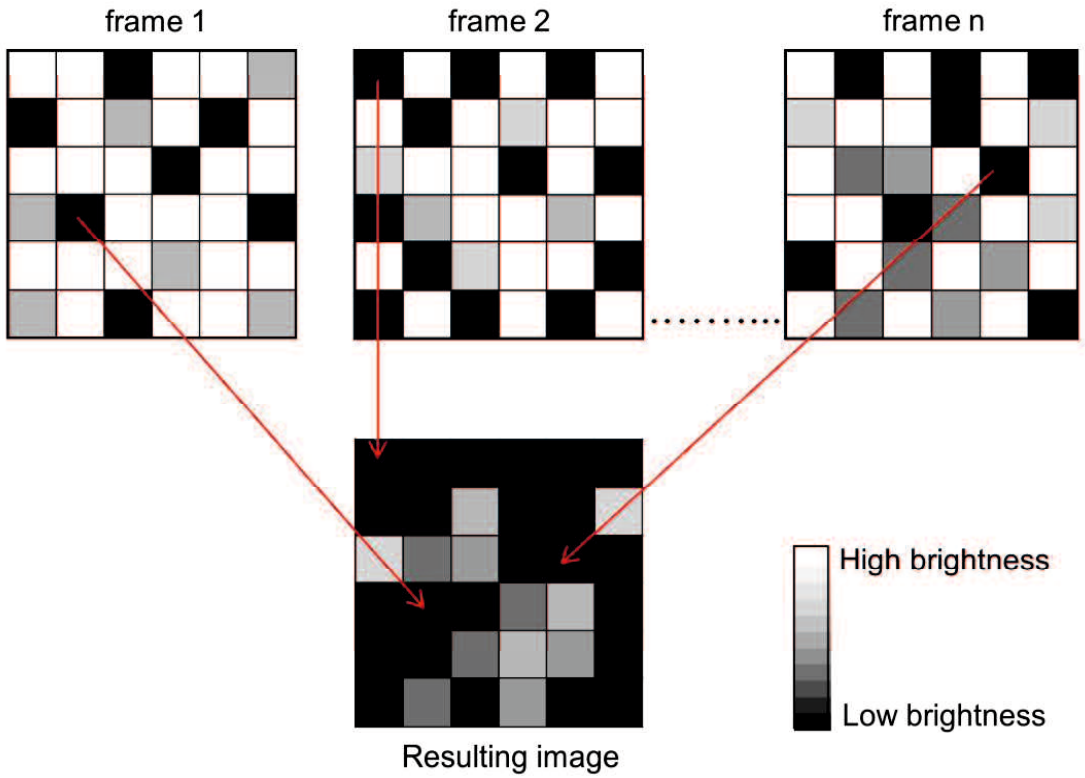

Figure 4-5. Illustration of temporal minimum filter.

4.2.5 Generation of shallow-water elevation map and bathymetric map

As the first step in this procedure, a dense point cloud at each site and for each technique was generated with a widely used SfM-MVS commercial software package, Agisoft PhotoScan version 1.2.6 (Section 2.3). To generate a shallow-water elevation map, first, the dense point cloud (prior to refraction correction) generated by SfM-MVS was extracted in the submerged areas. The triangulated irregular network (TIN) interpolation technique was applied to construct a two-dimensional model of the estimated bottom elevation for each site and technique. Finally, the TIN models were constructed to raster format in order to generate the shallow-water elevation map.

To generate a bathymetric map, first, a water surface elevation map was generated by interpolating the elevation points at the water's edge (measured from the RTK-GPS receiver) using the trend model. The shallow-water elevation map was then subtracted from the water surface elevation map to generate a bathymetric map.

4.2.6 Application of the proposed method

The overall workflow of the proposed method is summarized in this section. First, the drone was ordered to take a short –video (3 second) of each waypoint rather than still picture. The video recording was then corrected from the effect of the displacement and rotation of the camera, caused by the movement of UAV. To remove the effect of the reflection, the temporal minimum filter (a filter that extracts the smallest RGB value for each pixel from the available video frames) was applied to the video recording at each waypoint. The corrected images (free from reflection effect) were then used as the input in the SfM- MVS algorithm to generate the water –bottom elevation map and bathymetric map. The workflow of the proposed method is summarized in Figure 4-6.

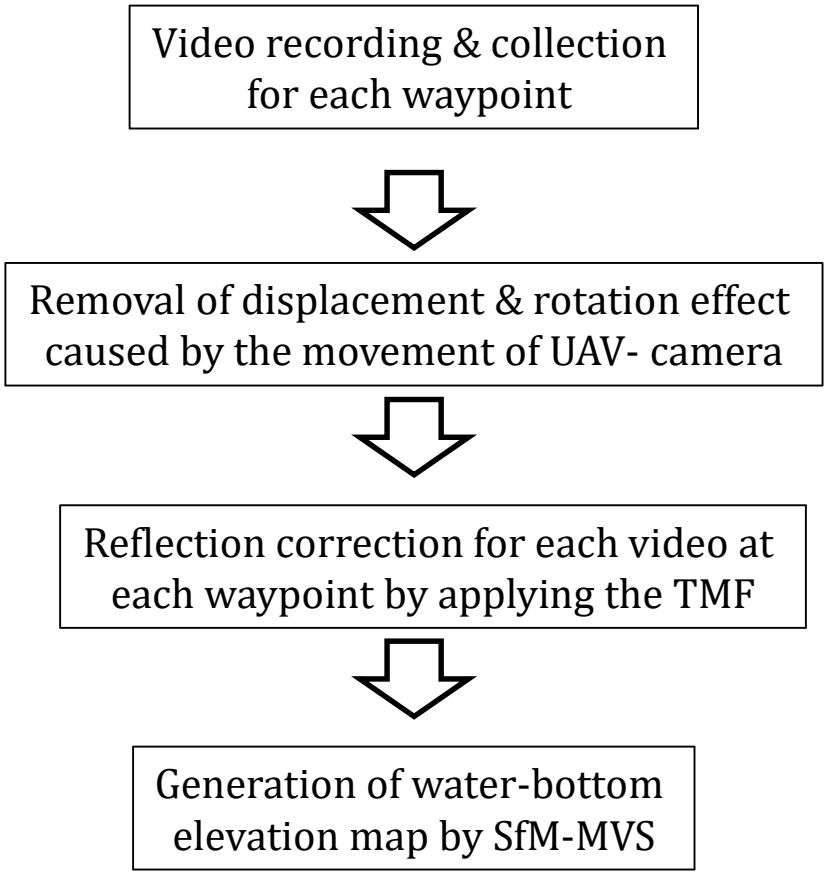

Figure 4-6. Workflow of the reflection correction by applying the proposed method.

4.2.7 Application of the refraction correction

Elevations of underwater points in the dense point cloud are overestimated by MVS, due to the refraction of light at the air–water interface. The bottom elevation of each point was corrected for the refraction effect by multiplying the apparent water depth by an empirical factor, as described in Partama et al. (2017). The empirical factor was estimated using five points of training data, randomly chosen in the framework of cross validation described below.

4.2.8 Evaluation of point densities

The dense point cloud generated from SfM–MVS was extracted in the submerged part of the main target area for each site and technique. The overall density of the point cloud was then calculated in the main target area (points/m^2),

and a map of the local point density (density in a 1-m square cell) was created for each technique at Site 1. Furthermore, the overall density and local point density of the two techniques were compared.

4.2.9 Accuracy evaluation for point cloud

In order to evaluate the accuracy and precision of photogrammetry with each technique, the measured elevation of the validation points (the underwater points where the world coordinates were measured by GNSS or TST) were compared with the mean corrected bottom elevation of the nearby points in the dense point cloud. The difference between these elevations was defined as the error of bottom elevation estimation by SfM–MVS.

In this approach, not all the validation points (the points where the world coordinates were measured by GNSS or TST) could be used for the accuracy and precision evaluations, because some are far from any point in the dense point cloud. In addition, I intended to focus my evaluation on the validation points in the "well applicable area" of each method, where the dense point cloud is sufficiently dense and the elevations of nearby points in the cloud are consistent. Therefore, I only used validation points (hereafter called "valid validation points") that have two or more points of the dense point cloud with small elevation variation (with standard error less than 0.1 m or 0.01 m) and within one pixel distance at the drone's home point (0.01 m for all sites) in the input image. I performed the evaluation for two standard error thresholds, 0.1 and 0.01 m, to verify that the superiority of the proposed technique is independent of the threshold. Even though the latter threshold may seem excessively severe, a significant number of validation points exceeded this level, as shown below. Overall, this approach only indicates the precision under ideal conditions and does not provide a measure of the overall survey accuracy.

The error statistics of mean corrected bottom elevation estimates for valid validation points were compared to assess the relative accuracy and precision of the two techniques. Because the refraction correction described above requires some training data to calibrate the empirical correction factor, a cross validation,

consisting of 1000 calibration/prediction trials was performed. In each trial, the available underwater measured points were randomly split into training (five points) and test data (all remaining points). The RMS of the prediction errors for the 1000 trials was evaluated for each site and technique.

4.2.10 Accuracy evaluation for bathymetric map

The accuracy of the bathymetric map after the refraction correction was performed by performing a similar cross validation to that described in the previous paragraph. The only difference was that, in this case, the measured elevation of each validation point was compared with the elevation of the pixel of the bathymetric map containing the point, rather than with the average elevation of the neighbour points of the dense point cloud. Moreover, through this approach, a measure of the overall survey accuracy, including the sparse area was obtained. For Site 2, some deep pixels of the bathymetric map derived from the normal technique had negative estimates of water depth. Those pixels were excluded from the accuracy evaluation, which favours the normal technique.

4.3 Results

4.3.1 Water bottom clarity

As demonstrated in Figure 4-7(b), compared with the normal technique (Figure 4-7(a)), the proposed technique reduced the water-surface reflection (sun glint) and the sea bottom looks significantly clearer. In addition, the moving light patterns (caustics) formed on the bottom surface by the waves (Figure 4-7(c)) were also diminished by this technique (Figure 4-7(d)).

4.3.2 Point densities

Figure 4-8 shows the dense point cloud generated by MVS in the submerged areas for each technique. Qualitatively, at Sites 1 and 2, it appears that the submerged region in the main target area is completely filled with the dense point cloud when the proposed technique is applied in the image retrieval step (Figure

4-8(b)). Furthermore, the validation points measured by TST (black triangles in Figure 4-8) were also fully covered by the dense point cloud (Figure 4-8(b)). On the other hand, the submerged area is not fully filled with the dense point cloud when the normal technique is used (Figure 4-8(a)).

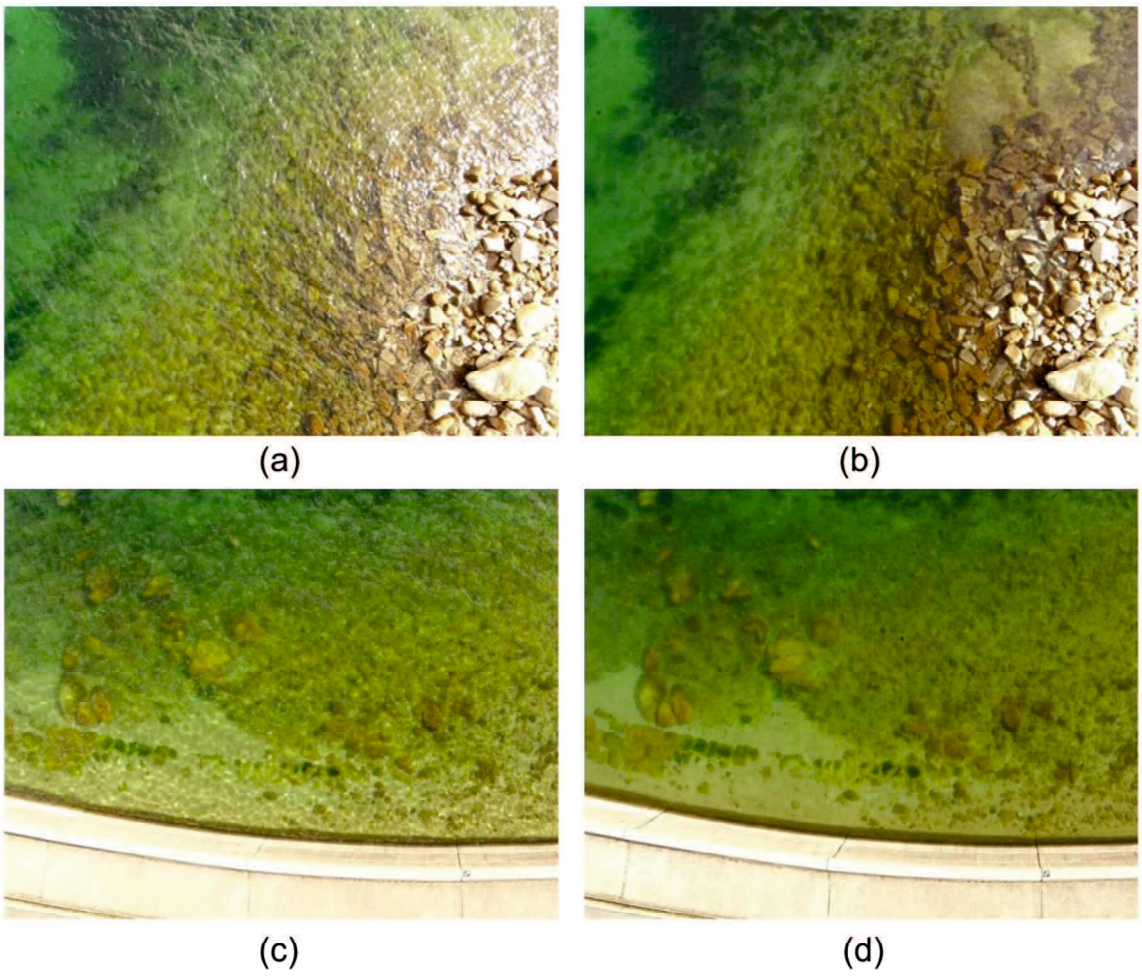

Figure 4-7. Images obtained with (a and c) randomly chosen frame and (b and d) proposed technique at Site 1.

At Site 3, the right bank side of the main target area is dominated by a large area of missing data, for both the proposed and normal techniques (Figures 4-7(a) and (b)); this missing data is caused by several factors: (1) the appearance of the sky reflection at the water surface in both input images (i.e., the images obtained using both the normal and proposed techniques), (2) lack of texture in the riverbed

(dominated with sand and lack off stone), and (3) the bottom reflectance is very poor (deep area and cloudy days).

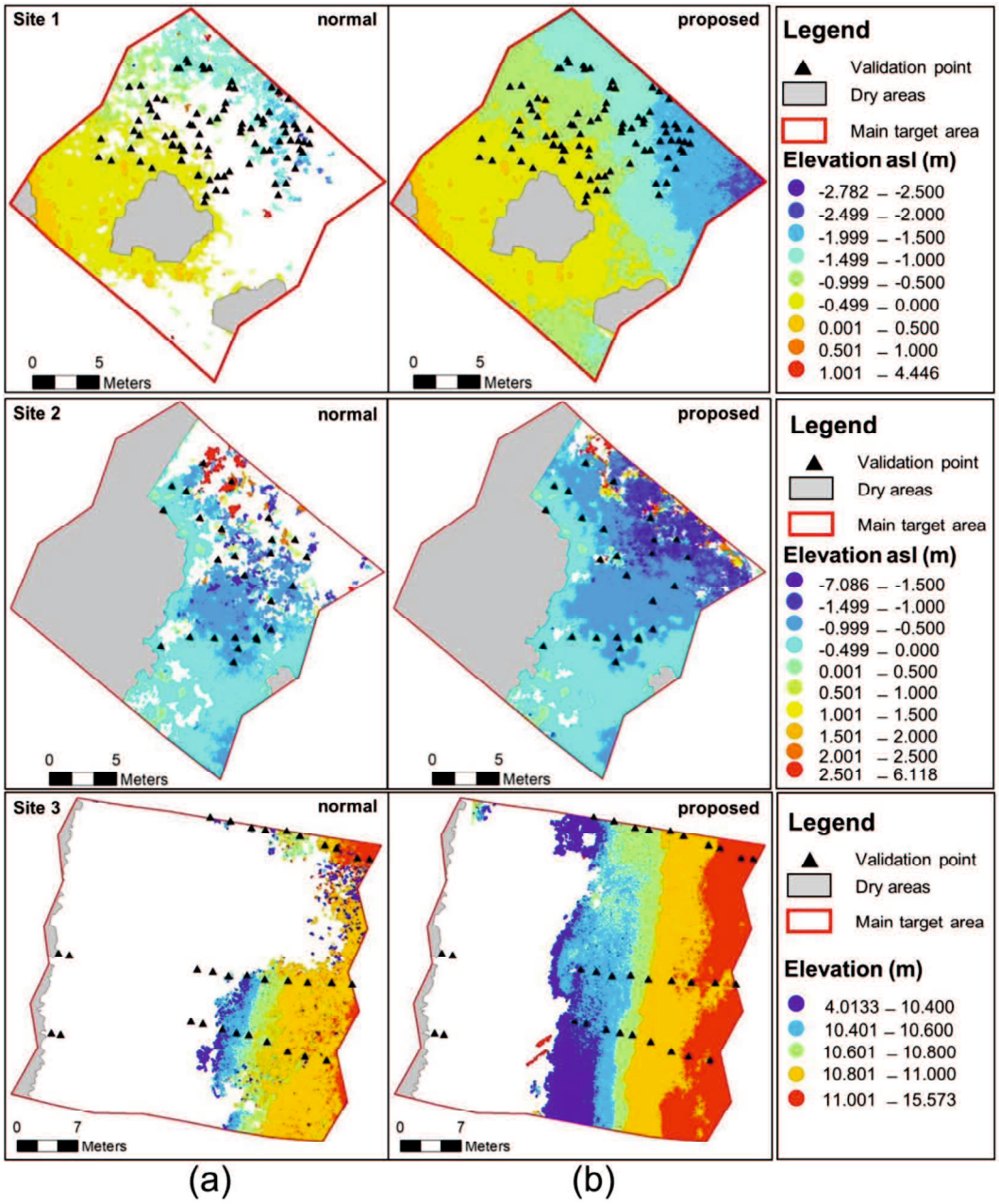

Figure 4-8. Dense point cloud generated using (a) normal technique, and (b) proposed technique, in submerged part of main target area at Sites 1, 2, and 3. The colored areas represent the point clouds.

On the other hand, on the left bank side, which is shallower and more abundant bottom texture (dominated with gravel and cobble) compare with the

right bank, the submerged area of the main target area is completely filled by a dense point cloud following application of the proposed technique (Figure 4-8(b)). In contrast, the corresponding area for the results obtained using the normal technique is not fully filled (Figure 4-8(a)).

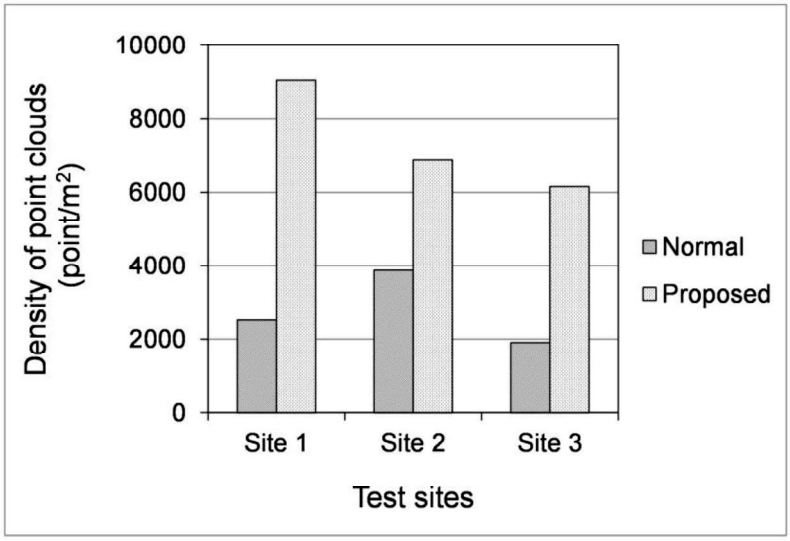

Figure 4-9. Density of point clouds for each technique and site in main target area.

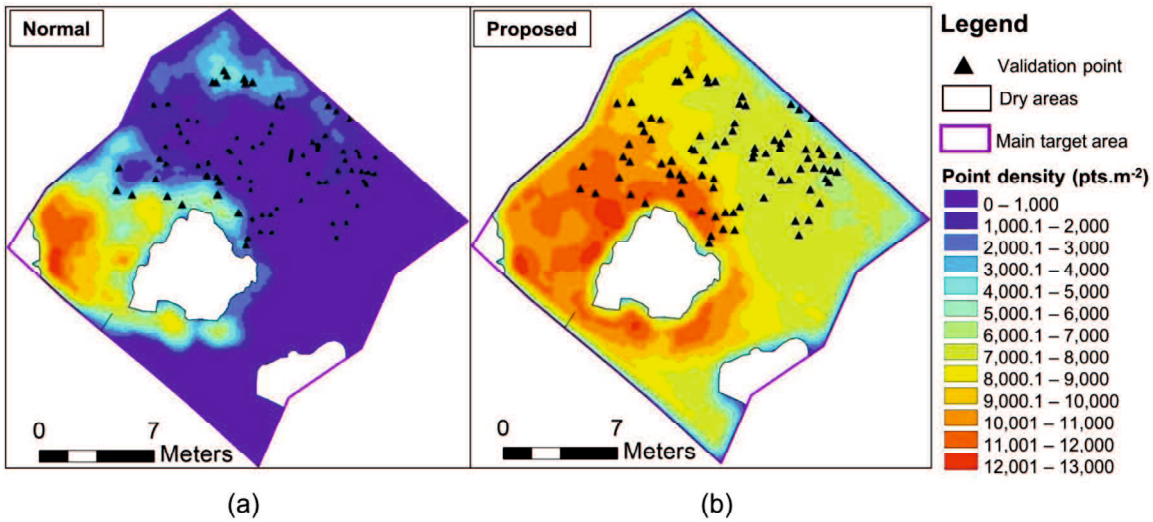

Figure 4-10. Spatial distributions of local point densities generated using (a) normal technique and (b) proposed technique, in submerged part of main target area at Site 1.

Quantitatively, applying the proposed technique increased the density of the point cloud by factors of 3.6, 1.8, and 3.2 at Sites 1, 2, and 3, respectively (Figure 4-9). Regarding the spatial distribution of the local point densities at Site 1 (Figure 4-10), the local point density increased in most parts of the submerged region of the main target area upon application of the proposed technique. Overall, these results show that the proposed technique improves the point density of UAV-based photogrammetry in submerged areas, by increasing the number of matching points between images in the SfM-MVS algorithm (Figure 4-11).

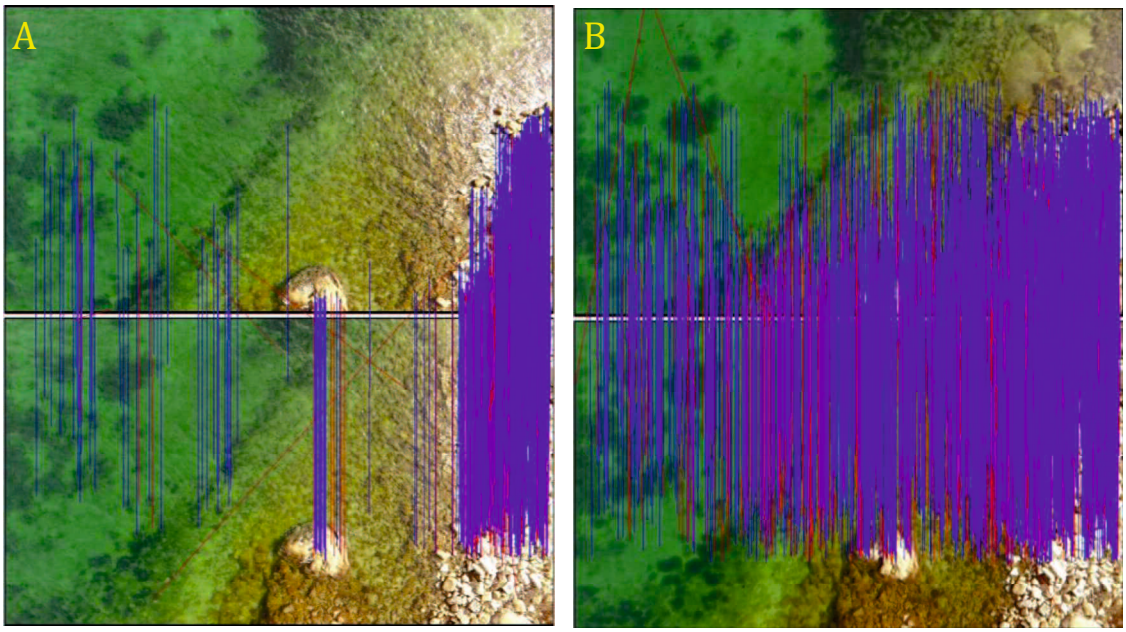

Figure 4-11. Features matching between overlaps images by applying (A) normal technique, and (B) proposed technique, at Site 1. (blue lines are connecting valid matching points; while red lines are connecting invalid matching points).

4.3.3 Point accuracies

Figure 4-12 shows scatter plots of estimated (after application of the refraction correction) vs. measured water depth at the valid validation points for each site. The proposed technique improved the correlation between the estimated and measured water depths at the three test sites, indicated by the greater coefficient of determination (R^2) at each site following usage of the proposed technique.

At Site 2 (top graph in Figure 4-12 (b)), I found an outlier with large negative bias (red point) when I applied the normal technique. Visual inspection of input images indicated that this outlier was located where the water-surface reflection was significant in some images. The magnitude of this bias was greatly reduced by the proposed technique (bottom graph in Figure 4-12 (b)).

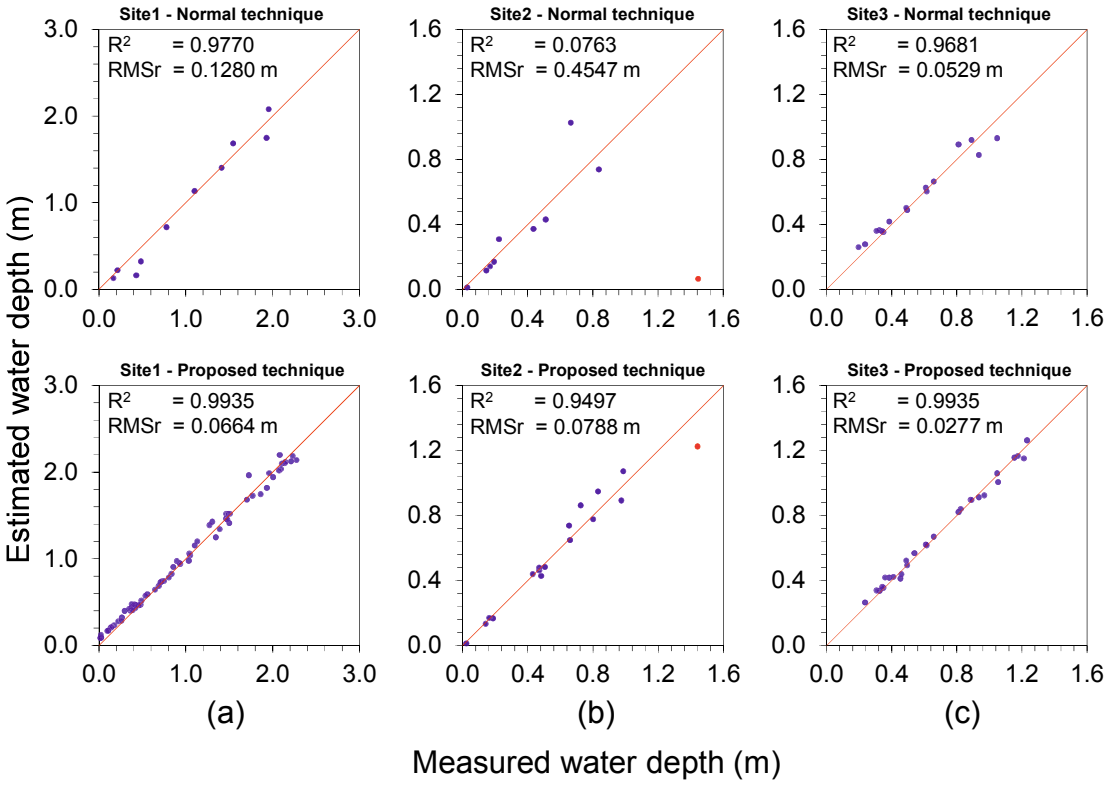

Figure 4-12. Scatterplots of water depth estimated by SfM–MVS versus water depth measured by TST or RTK–GPS for all valid validation points after application of refraction correction procedure, at Sites (a) 1, (b) 2, and (c) 3, without (above) and with (below) application of proposed technique. RMSR indicates root mean square residuals; here, the residual corresponds to the estimation error for the training data (the data used to adjust the refraction correction factor).

Table 4-3 and Table 4-4 list the number of valid validation points and the RMSE of the mean corrected bottom elevation for the points for each site and technique. In addition to the statistics for all the valid validation points, I also show statistics for the valid validation points commonly available in two techniques. I

use a standard error threshold of 0.10 m in Table 4-3 and 0.01 m in Table 4-4 to define the valid validation points.

Table 4- 3. Number of valid validation points (with stable dense points in the neighborhood) and the RMSE of the mean corrected elevation obtained by cross-validation using all valid points or only the common valid points of the two methods (when 5 points were used for calibrating the empirical water-surface gain-only refraction correction) with a standard error threshold of 0.10 m.

Field test case	Technique	Number of measured points by GPS & total station	Measured points with multiple neighbors		All valid validation points		Commonly valid validation points	
			Number	Standard error [m]	Number	RMSE [m]	Number	RMSE [m]
Site 1	Normal	92	11	0.007	11	0.143	10	0.147
	Proposed		72	0.005	72	0.078		0.064
Site 2	Normal	55	10	0.013	10	0.464	9	0.492
	Proposed		19	0.041	17	0.085		0.097
Site 3	Normal	35	16	0.002	16	0.057	15	0.056
	Proposed		28	0.001	28	0.031		0.020

Table 4-3 shows that, with the proposed technique, the RMS error decreased by a factor of 1.8 at Site 1; 5.5 at Site 2; and 1.8 at Site 3 (for all valid validation points), and 2.3 at Site 1; 5.1 at Site 2; and 2.8 at Site 3 (for commonly valid validation points). Table 4-4 shows comparable improvement with the proposed technique and a standard error threshold of 0.01 m, except for the common validation points at Site 2. Based on visual observation of each input image, I suspect that the lower accuracy and precision of the proposed technique

compared with the normal technique at Site 2 might be due to the absence of water-surface reflection at the common validation points.

Table 4- 4. Number of valid validation points (with stable dense points in the neighborhood) and the RMSE of the mean corrected elevation obtained by cross-validation using all valid points or only the common valid points of the two methods (when 5 points were used for calibrating the empirical water-surface gain-only refraction correction) with a standard error threshold of 0.01 m.

Field test case	Technique	Number of measured points by GPS & total station	All valid validation points		Commonly valid validation points	
			Number	RMSE [m]	Number	RMSE [m]
Site 1	Normal	92	9	0.134	7	0.122
	Proposed		64	0.074		0.065
Site 2	Normal	55	8	0.505	7	0.026
	Proposed		15	0.064		0.055
Site 3	Normal	35	16	0.057	15	0.056
	Proposed		28	0.031		0.020

4.3.4 Bathymetric mapping accuracy

Figure 4-13 shows scatter plots of estimated (after application of the refraction correction) vs. measured water depth for bathymetric map at each site. The proposed technique improved the correlation between the estimated and measured water depths at the three test sites, indicated by the greater coefficient of determination (R^2) at each site following usage of the proposed technique. This result shows the comparable improvement with the accuracy of point clouds as shown in the previous section.

Table 4- 5. Error statistics of bathymetric map for each technique and each site.

Field test case	Technique	Total number of validation points	Number of validation points with missing data	Number of validation points with negative apparent depth	Number of common validation points	Error statistics of common validation points [m]			
						Mean error	Standard deviation of errors	Mean absolute error	RMSE
Site 1	Normal	92	0	0	92	–0.036	0.300	0.225	0.302
	Proposed		0	0		0.013	0.078	0.061	0.079
Site 2	Normal	55	14	20	21	–0.048	0.442	0.255	0.444
	Proposed		2	0		–0.001	0.152	0.095	0.152
Site 3	Normal	35	4	0	31	0.009	0.136	0.104	0.137
	Proposed		4	0		0.006	0.053	0.040	0.054

The error histogram (Figure 4-14) and error statistics (Table 4-5) of the bathymetric map show that the bias (mean error) and noise (standard deviation error) decreased upon application of the proposed technique at Sites 1, 2, and 3. Similarly, the mean absolute error (MAE) and RMSE also decreased upon application of the proposed technique (Table 4-5).

At Site 2, for the normal technique, some validation points have a negative apparent depth value (Table 4-5). Based on visual observation of each input image, this estimation error may be due to the appearance of water surface reflection at the validation points. On the other hand, no validation points with negative values were obtained when the proposed technique was applied.

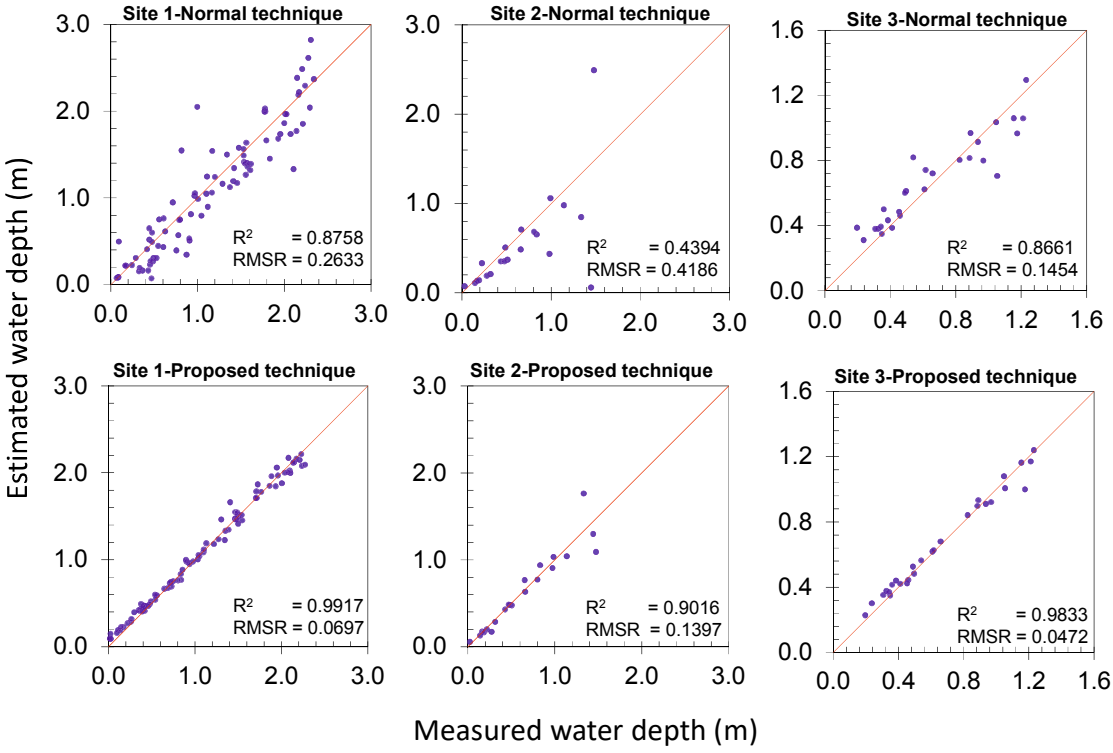

Figure 4-13. Scatterplots of water depth estimated by SfM–MVS versus water depth measured by TST or RTK–GPS for bathymetric map after application of refraction correction procedure, at Sites (a) 1, (b) 2, and (c) 3, without (above) and with (below) application of proposed technique.

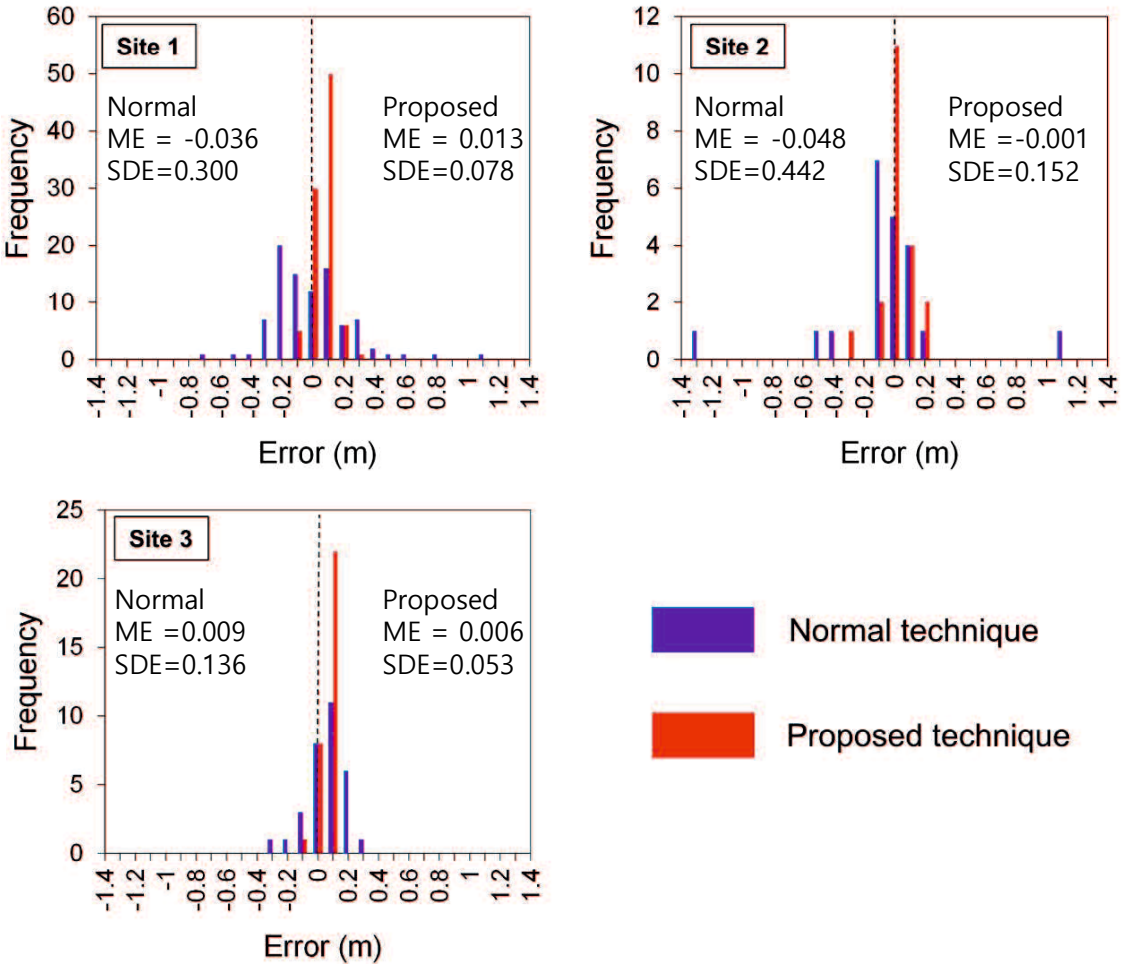

Figure 4-14. Distribution of depth errors for each technique at Sites (a) 1, (b) 2, and (c) 3.

Figure 4-15 shows the DEM generated by applying the normal (Figure 4-15 (A)) and proposed techniques (Figure 4-15 (B)) in the submerged part at Site 1. Based on visual interpretation, the coverage area of DEM increased upon application of the proposed technique. In addition, the DEM generated from proposed technique is more realistic compared with the normal technique, specifically in the areas which suffered from water surface reflection effect. In summary, the proposed technique improves the accuracy and precision of UAV-based shallow water photogrammetry by reducing the effects of water-surface reflection.

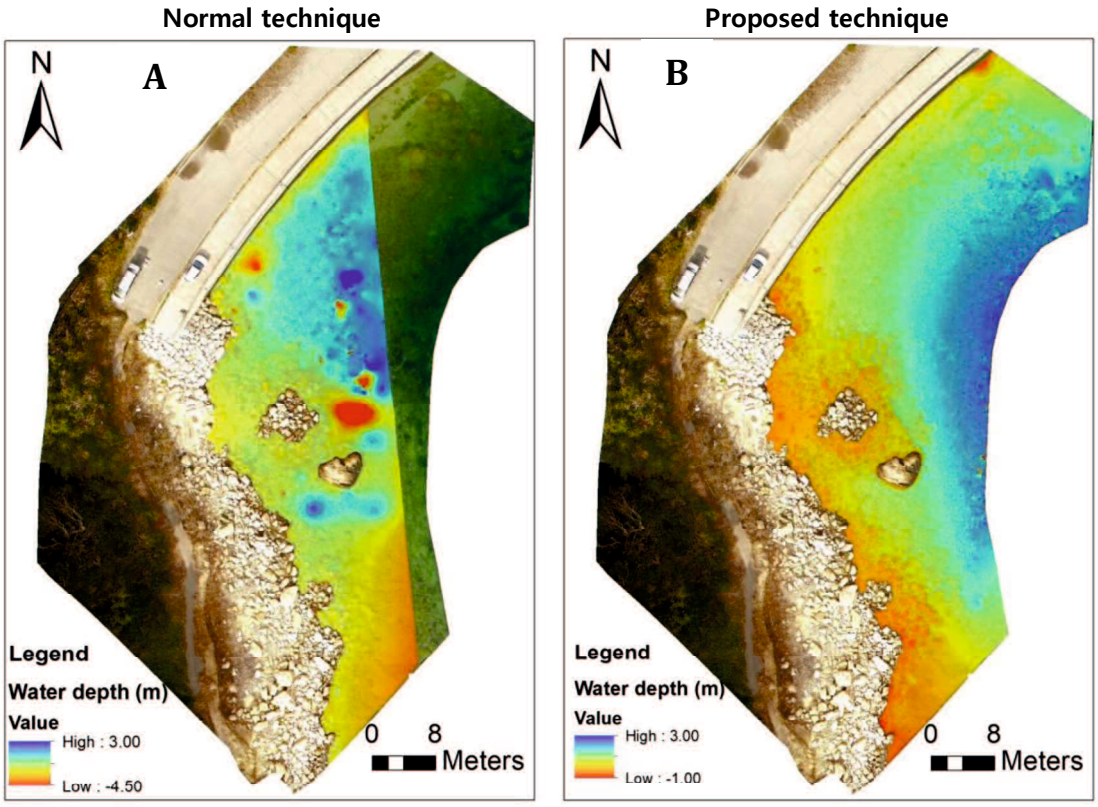

Figure 4-15. Examples of the DEM generated by normal (A) and proposed (B) technique at Site 1.

4.4 Discussion

4.4.1 Applicability of proposed technique

This study has described development of a procedure for reflection filtering at the water surface to map shallow-water topography based on SfM-MVS photogrammetry. Three small tests of this procedure in coastal and river areas showed its significant effectiveness in improving the accuracy and precision of UAV-based shallow-water photogrammetry, although the test sites in this study were small.

The advantage of this procedure is direct removal of the sun/sky reflection from imagery, a technique that has not been established in the classical or SfM-MVS photogrammetry fields. In some previous works, reflection was minimized through careful flight planning (Cassella et al., 2016; Dietrich, 2016). However, this method may limit the surveying time and may only be applied on sunny days. On

the other hand, the technique developed in this work provides an approach to accommodating reflection removal under all illumination conditions, as the proposed technique produces accurate bathymetric measurements under both sunny and cloudy conditions (Results).

Westaway et al. (2001) addressed water-surface reflection by manually eliminating point clouds in which the photogrammetry was assumed to have failed to detect the bottom. This method may be applied only when the reflection on the water surface is insignificant and the areas that contain the reflection are very small. On the other hand, our proposed technique provides a method for removing significant reflection in imagery involving large reflection coverage on the water surface, as demonstrated in Figure 4-6(b).

Although the applicability of the proposed technique was found to be superior to alternative methods in some cases, the proposed technique is more time consuming in the air than the existing UAV-based shallow-water photogrammetry techniques presented in some works (Woodget et al., 2015; Casella et al., 2016; Dietrich, 2016, Partama et al., 2017). This time difference arises because, in the video collection stage, the proposed technique requires the UAVs to stop and hover for a few seconds at each waypoint to record video. In this study, the time periods required for video collection at Site 1 (main target area: 400 m^2) and at Site 3 (main target area: 1200 m^2) were 11.5 and 20.5 min, respectively.

In this study, the accuracy of bathymetric mapping will not affected by the systematic bias due to limited choice of the orientation of water surface slope tilting by temporal minimum filter. There are two reasons: 1) according to Fresnel reflectance (Table 1, Appendix), the change of the reflectance (water surface reflectance of sun/sky) depending on the water surface orientation is small. For example, as shown in Figure 4-16, when the drone position is 30^0 from zenith and the water surface tilting is from -5^0 to 5^0 , then the incidence angle of sky light reflection vary from 20-40^0, but that change is only change the Fresnel reflectance just by 0.4% (Table 1, Appendix). However, if there is some cloud patches and inhomogeneity in color in this range, the color diversity is more than 0.4%. This

means, the inhomogeneity in the sky light will be the more important factor compare with water surface reflectance change due to the tilting. 2) When the intensity of reflected sky light increases due to the slight increase in Fresnel reflectance due to the larger incidence angle cause by tilted water surface toward the direction of the drone, bottom light penetration will slightly decrease. It's mean the total intensity of bottom and sky light may not increase. Whether it increases/decreases depend on the intensity of sky/sun light.

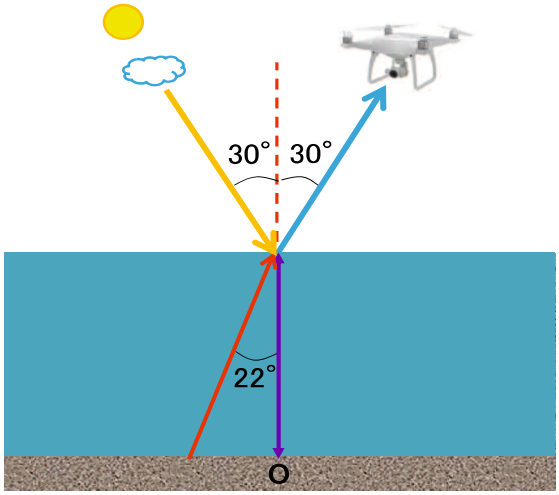

(a) Water surface slope angle is level

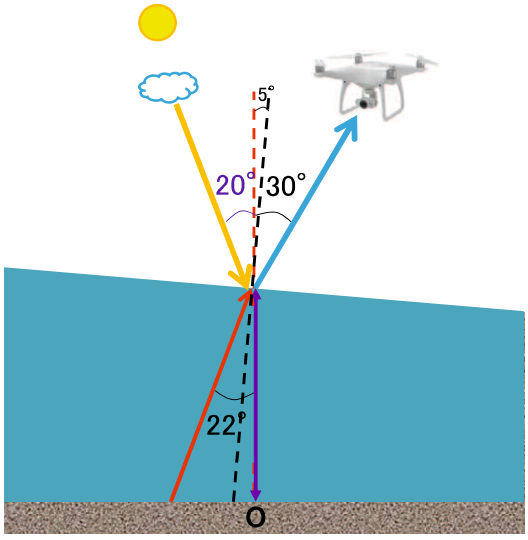

(b)Water surface slope angle tilted by 5^0

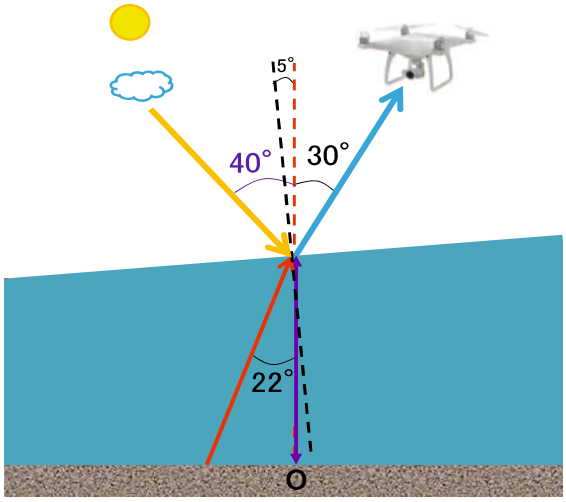

(c) Water surface slope angle tilted by -5^0

Figure 4-16. Geometry of incident and reflected lights as a function of water surface slope orientation (tilting).

4.4.2 Accuracy comparison

The error statistics (Table 4-5) indicate that the proposed method yields higher accuracy (0.05-0.15 m) than the techniques reported by Mandlburger et al. (2016) and Flener et al. (2013) for remote surveying of shallow-water bathymetry. Mandlburger et al. (2016), who used a UAV-borne topo-bathymetric laser profiler (ground resolution: 0.01 m), reported an accuracy of 0.16 m, whereas Flener et al. (2013) reported accuracies of 0.08 to 0.22 m using UAV-based color-depth bathymetric modelling (ground resolution: 0.05 m). On the other hand, in the terrestrial laser scanning survey performed by Smith et al. (2011) (ground resolution: 0.01 m), accuracy (0.05 m) comparable with the proposed method was obtained.

4.4.3 Another application and additional benefit

The method for removal of water-surface reflection presented in this study could also be useful for costal and fluvial remote sensing applications. The visibility of the bottom bed in the imagery is improved (Figures 4-7(b) and (d)), yielding improvement in the accuracy of the bathymetric measurement; this suggests that the proposed technique clarifies the reflected signal from the bottom bed. This clarification could improve the accuracy of benthic habitat mapping in coastal remote sensing applications as well as the accuracy of bottom sediment classification in fluvial remote sensing applications.

While this study focused on the manner in which the TMF can remove the reflection effect in the image retrieval step, the TMF could also be useful for image refinement, especially removal of unusually bright pixels from imagery. As an additional benefit obtained by applying this technique, the moving light patterns (wave caustics) could diminish on a shallow-water bed, as shown in Figure 4-7(d). This effect causes significant problems during image point matching in the photogrammetry procedure, leading to the generation of outliers during dense point cloud generation (Grenzdörffer and Naumann, 2016).

4.4.4 Limitations

The proposed technique has several limitations, the most important of which is that its effectiveness depends on the wave state conditions. When the wave is very small (low water-surface roughness), the light rays reflected from the water surface travel in the same direction (to the camera sensor) during video recording. This condition causes the appearance of sun/sky reflection in each succeeding frame in a set video. In this case, the TMF does not effectively remove the water surface reflection, yielding insufficient point-cloud density in UAV-based shallow-water photogrammetry. For this reason, the proposed technique may not be applicable to removal of the water surface reflection effect in areas with low water-surface roughness.

Imaging through a dynamic water surface can be affected by different types of degradation, one of which is geometric distortion due to unidirectional cyclic waves. This effect causes an underwater object to appear to be moving over time, appearing in its neighbouring pixel cells in a video recording. The magnitude of the movement of the underwater object depends on the distance between the camera and water surface as well as the water depth. If this distance is very short and the water depth is large, the object movement is very significant. This movement causes the TMF to enlarge the underwater object (especially for low-brightness objects) contributing to the blurring effect in the corrected image and inducing point feature mismatching in the photogrammetry procedure. Although the proposed technique suffers from this negative effect, it still provided superior results to the normal technique in this study. This indicates the strong benefit of water surface reflection removal as a key factor for improving the accuracy of UAV-based shallow-water photogrammetry.

4.5 Summary and Conclusion

In this study, a new imaging technique that reduces the effect of water-surface reflection on UAV-based shallow water photogrammetry was presented. In this technique, the UAV was ordered to take a few seconds of video instead of a still picture at each waypoint. The temporal minimum filter (a filter that extracts the

smallest RGB value for each pixel from the available video frames) was then applied to the video in order to obtain an image with reduced intensity of reflection of sun and sky at the water surface. In order to assess the effectiveness of this method, it was tested in three experiments in a river and at the coast, and compared the point-cloud density, accuracy, and precision of the water bottom elevation generated by SfM–MVS with those generated from a randomly chosen frame. As a result, the presented technique achieved a much denser point cloud than that derived from the randomly chosen frame. The presented technique also showed better overall accuracy and precision in determining the water bottom elevation. The effectiveness of the proposed technique should depend on the surface wave state and sky radiance distribution.

Chapter 5. Discussion and Conclusion

5.1 Summary of key findings

The water surface refraction/reflection correction methods within this thesis has been shown to be capable to improve the accuracy and precision of UAV-based shallow-water bathymetric mapping, although with certain limitations determining where and when it perform best. A summary of the key findings is presented within this section, with a focus on the results of a quantitative assessment of accuracy and precision for bathymetric mapping.

A. Water surface refraction correction

Generally, higher accuracy and precision data were produced for exposed area (RMSE = 0.03 m), as opposed to submerged area (RMSE= 0.08 m, where error scales with water depth). For submerged areas, the accuracy and precision of horizontal (X and Y) direction (RMSE= 0.05 m) is higher than vertical (Z) direction (RMSE= 0.13 m) , and indicate the importance of the refraction correction in that direction.

The application of a simple refraction correction method (CF=1.34, Westaway et al., (2001)) helped to reduce (by c. 40%) but still suffered from a significant systematic overestimation of estimated water depth. This demonstrates the geometrical fact, that a CF of 1.34 is the minimum possible value and is not enough in a real application. The both of linear correction methods (which estimate the gain and offset, and the proposed method) outperformed Westaway et al. (2001) method, when the training data used for calibration is large. The proposed method is superior of any other method in Site 2. Even in Site 1, the proposed method is still superior when the number of submerged point measurement was very small. Method 4, which has two degrees of freedom in the correction formula, yielded extremely large errors when the number of training data was very small (less than five). This is statistically natural: the more degree of

freedom a regression model has, the more unstable are the estimates of the coefficients, and the model requires more training data to function well. The best linear correction method depends not only on the number of training data but also many other factors, such as site locations, image acquisition conditions, GPS measurement conditions, and so on.

B. Water surface reflection correction

The water surface reflection correction method by applying a temporal minimum filter, significantly reduce the water-surface reflection effect (sun glint) and improved the visibility of the bottom bed in the imagery. This improvement could increase the features matching in SfM-MVS algorithm, yielding improvement in the density of dense point cloud (by factor more than 1.5), as well as improvement in the accuracy and precision of UAV-based shallow-water bathymetric mapping (the RMSE decreased by factor more than 1.5) in all sites. The effectiveness of the proposed method is depends on many factors, such as the surface wave state conditions, atmospheric conditions, water depth, flying height of UAV, and water bottom textures.

The video stabilization technique was effectively reduce the effect of displacement and rotation caused by the movement of UAV camera (standard deviation of the position of the object, originally more than 4 pixels, were reduced to sub pixel level).

Comparison with bathymetric products from other remote sensing approaches finds higher or slightly similar accuracy to proposed method. Higher accuracy and precision water depth data than obtained using UAV-borne topo-bathymetric laser profiler (Mandlburger et al., 2016) and UAV-based color-depth bathymetric modeling (Flener et al., 2013) are observed in nearly all sites. On the other hand, in the terrestrial laser scanning survey (Smith et al., 2012), the accuracy and precision was comparable with the proposed method.

5.2 Evaluation of the proposed method

This section aims to provide an overarching evaluation of the proposed methods for water surface refraction/reflection correction in UAV-based shallow-water photogrammetry. The key benefits and limitations are discussed, with a focus on the wider, practical applicability of the methods.

5.2.1 Advantages

A. Water surface refraction correction

1. **The proposed method is more practical and easy to implement compare with the geometrical refraction correction method**. The geometrical approaches requires the information about the position of the camera coordinates, which the common photogrammetry software does not output this information. In addition, the geometrical refraction correction approach for multi-view stereo cases is more complex compare with single/stereo-view cases.
2. **The empirical linear correction approach that estimates a reasonable correction factor for a specific flight by minimizing the total error (RMSE) is not only correct for the effect of water surface refraction.** This linear regression method is sometimes correct for the systematic error due to incorrect estimation of camera intrinsic and extrinsic parameters by SfM algorithm.
3. **The proposed method is more stable (robust) than the Method 4 in estimating correction factor when the estimated apparent water depth is noisy.** This indicates the superiority of the proposed method in terms of the geometric soundness of the estimated CF.

B. Water surface reflection correction

1. **The proposed method provides an approach to accommodating reflection removal under all illumination conditions.** As explained in the Results section, the proposed method produces accurate bathymetric

measurements under both sunny and cloudy conditions. This means the proposed method is more applicable than the existing methods, which does not limit the surveying time (except for night time).

2. **The proposed technique provides a direct removal of the sun/sky reflection from imagery that has not been established in the classical or SfM-MVS photogrammetry fields**. As a result, this method capable to remove the significant reflection in imagery involving large reflection coverage on the water surface.
3. **Clarification of the water column signal could benefit remote sensing applications targeting water quality parameters such as turbidity and suspended sediment (e.g., Kilham et al., 2012).**
4. **Clarification of the bottom reflected signal could improve substrate and benthic mapping as well as bottom classification efforts.** More generally, removal of sun glint will improve histogram-based channel classification operations in which bright, sun glint contaminated pixels are often erroneously classified as non-water.

5.2.2 Limitations

A. Water surface refraction correction

1. An important limitation of linear correction method of inferring shallow-water bathymetry using photogrammetry is the need for field measurements of depth to calibrate the empirical linear correction formula, which often precludes application of this method to monitor a wide area.
2. Field measurements ideally would be obtained at the same time the image is acquired, particularly in dynamic channels and/or where changes flow stage are significant. If field and image data are not collected simultaneously, changes in depth, if not the morphology of channel itself, can biased estimated of CF. Coordinating filed crews with flight operations involves a number of logistical challenges, however, and perfect timing is difficult to achieve in practice.

3. The refraction correction factor obtained via regression against field measurements are site and scene specific, and might not be applicable to other sites and data sets.

B. Water surface reflection correction

1. The proposed method is more time consuming in the air than the existing UAV-based shallow-water photogrammetry approaches presented in some works. This time difference arises because, in the video collection stage, the proposed method requires the UAVs to stop and hover for a few seconds at each waypoint to record video.
2. The video recording are affected by video encoding/decoding artifacts (blurring, blocking, ringing, etc.) that caused the quality of the resulted TMF image became poor and reduce the accuracy and precision of UAV-based shallow-water photogrammetry.
3. The effectiveness of the proposed method is depends on the wave state conditions. The TMF does not effectively remove the sun/sky reflection, when the wave state is nearly to be level (very low water-surface roughness), yielding insufficient point-cloud density as well as accuracy of UAV-based shallow-water photogrammetry.
4. The resulted TMF images of submerged areas are suffers from another cause of blurring, i.e., apparent motion of the underwater points due to surface waves. The magnitude of this effect is depending on the water depth and the altitude of UAV from water surface.

5.3 Recommendations for future work

It is important that future research efforts are channeled into developing methods for overcoming the limitations of the water surface refraction/reflection correction methods which have been highlighted by this research. The recommendations for future work of these proposed methods are described below:

A. Water surface refraction correction

1. **Development of refraction correction method which used a single correction factor to calibrate the estimated water depth.** This research has been focused on a linear correction method which required the field measurements to calibrate the correction formula. Future research is required to improve the practicality of the refraction correction method by developing a method which only used an optimal correction factor to calibrate the water depth.
2. **Investigation of the error due to incorrect estimation of intrinsic and extrinsic parameters by SfM algorithm is needed**; to know how large this error affects the accuracy of UAV-based shallow-water bathymetric measurement.
3. **Addressing the challenges of data acquisitions**. To improve the quality of the bathymetric model, further research might explore optimum levels of image overlap rate, flying altitude, camera orientation (e.g., off nadir view) and ground control point settings (e.g., densities and configurations). The results of this experiment would assist in the planning of efficient data acquisition campaigns.

B. Water surface reflection correction

1. **Addressing the challenges of data acquisition**. Further research might explore optimum levels of recording time, camera settings (frame rates, ISO, and shutter speed), flying height, and image overlap, the results of which would assist in the planning of efficient data acquisition campaigns.
2. **Development of video correction techniques to improve the quality of video recording**. The quality of the resulted TMF images depends on the quality of the video recordings. The quality of video recordings sometimes reduced due to blurring effect and other video encoding/decoding artifacts. The development of video processing technique to reduce these effects should be enhanced in future to improve the quality of bathymetric model.

3. **Testing the applicability of this approach over large areas of survey.** This research has been focused on quantification of a physical geomorphological feature (water depth) in a small area of survey (which were only about 100 m^2). Further work is required however to demonstrate the utility of the proposed method in the large area of survey.
4. **Testing the applicability of this approach for other remote sensing applications.** Future research is required to demonstrate the applicability of proposed method for a real-world, practical applications, because a number of potential applications arise from this research (such as: coastal benthic and bottom sediment mapping and water quality assessment).

5.4 Final conclusion

The recent development of UAV-based Structure-from-Motion (SfM) and Multi-view Stereo (MVS) photogrammetry techniques, which is an automatic image-processing-based computer vision technology, has provided the opportunity for low-cost bathymetric data acquisition. However, the applicability of this technique is limited by water surface refraction/reflection effects. As a consequence, the methods to correct these effects are required to improve the accuracy and precision of bathymetric measurement. The research presented within this thesis aimed to assess the capabilities of the relatively novel approach of water surface refraction/reflection correction for achieving just that.

This research has demonstrated that a water surface refraction correction approach by using Least Square method (which has one degree of freedom in the linear regression formula) can be used to improve the accuracy and precision of UAV-based shallow-water photogrammetry, albeit within certain constraints. Significant advantages over existing approaches include the capability of this approach to correct the refraction effect and other negative effects in the photogrammetric measurement (such us unknown error source within photogrammetry software), simultaneously. In addition, the proposed method is more practical and easy to implement compare with the geometrical refraction correction method. Compare with another linear correction approach (which has

two degrees of freedom in the correction formula); the proposed method was superior in all sites when the training data is small. In terms of geometric soundness of the estimated correction factor, the proposed method is more stable (robust) than another linear correction method in estimating correction factor when the estimated apparent water depth is noisy. However, an important limitation of linear correction method of inferring shallow-water bathymetry using photogrammetry is the need for field measurements of depth to calibrate the empirical linear correction formula, which affects the applicability of this proposed method.

Application of the water surface reflection correction approach developed within this thesis at three different research sites has enabled to improve the quality of the input images (especially in the submerged parts). This improvement leads to increased point cloud density (by factor of 1.8 - 3.6), as well as improved the accuracy and precision of UAV-based shallow-water bathymetric measurement (the RMSE reduced by factor of 2.5 – 3.8). The proposed technique provides a direct removal of the sun/sky reflection from imagery that has not been established in the classical or SfM-MVS photogrammetry fields. In addition, the proposed method provides an approach to accommodating reflection removal under all illumination conditions. However, the accuracy, precision and reliability of results is shown to be variable within and between different research sites, and the ability to produce consistently high quality outputs has not yet been proven. A number of critical limitations relating to data acquisition (including the recording time and wave state conditions), data processing (including the blurring effect due to wave motion and video encoding/decoding artifacts) and small spatial test areas have been identified. The recognition of these limitations has highlighted a number of important areas for future work.

Ultimately, the water surface refraction/refraction correction approaches has potential as a valuable tool for improving the effectiveness of UAV-based shallow-water photogrammetric measurement. The rapid and on-going developments in the UAS and sensor markets mean that increasingly powerful, more autonomous system are becoming available, capable of carrying heavier and

more complex sensors (e.g. multi-spectral sensors), flying in more challenging conditions and for longer times, enabling coverage of greater areas at hyper spatial resolutions. It is hoped that such improvements in UAS, in conjunction with further rigorous and dedicated quantitative assessments, will facilitate the development of the UAS-SfM approach to a point where it might be used for routine and reliable assessment of the quality and availability of shallow-water bathymetric assessment in future.

References

Agisoft PhotoScan. (2017). Agisoft PhotoScan User Manual: Professional Edition, Version 1.3

Bagheri, O., Ghodsian, M., & Saadatseresht, M. (2015). Reach scale application of UAV+SfM method in shallow rivers hyperspatial bathymetry. International Archives of the Photogrammetry, Remote Sensing and Spatial Information Sciences 40: 77-81.

Butler, J. B., Lane, S. N., & Chandler, J. H. (2002). Through-water close range digital photogrammetry in flume and field environments," Photogrammetric Record 17 (99): 419-439.

Carbonneau, P. E., & Dietrich, J.T. (2017). Cost-effective non-metric photogrammetry from consumer-grade sUAS: Implications for direct georeferencing of structure from motion photogrammetry. Earth Surface Processes and Landforms 42(3): 473–86. DOI:10.1002/esp.4012.

Carrivick, J., Smith, M., Quincey, D. & Carver, S., (2013). Developments in budget remote sensing for the geosciences. Geology Today, 29(4), 138–143.

Casella, E., Collin, A., Harris, D., Ferse, S., Bejarano, S., Parravicini, V., Hench, J. L., & Rovere, A. (2016). Mapping coral reefs using consumer-grade drones and structure from motion photogrammetry techniques. Coral Reefs 36: 269-275. DOI:10.1007/s00338-016-1522-0.

Dietrich, J. T. (2016). Bathymetric structure from motion: extracting shallow stream bathymetry from multi-view stereo photogrammetry. Earth Surface Processes and Landforms 42: 355-364. DOI:10.1002/esp.4060.

Eisenbeiß, H. (2009). UAV Photogrammetry. Dissertation, Institut für Geodäsie und Photogrammtrie, ETH Zürich, IGP Mitteilungen, 105.

Feurer, D., Bailly, J-S., Puech, C., Le Coarer, Y. & Viau, A.A. (2008). Very-high-resolution mapping of river-immersed topography by remote sensing. Progress in Physical Geography 32(4): 403-419.

Flener, C., Vaaja, M., Jaakkola, A., Krooks, A., Kaartinen, H., Kukko, A., Kasvi, E., Hyyppä, H., Hyyppä, J., & Alho, P. (2013). Seamless mapping of river

channels at high resolution using mobile LiDAR and UAV-photography. Remote Sensing 5: 6382-6407. DOI:10.3390/rs5126382.

Fonstad, M. A., Dietrich, J. T., Courville, B. C., Jensen, J. L. & Carbonneau, P. E. (2013). Topographic structure from motion: a new development in photogrammetric measurement. Earth Surface Processes and Landforms 38 (4): 421-430.

Fryer, J. G. (1983). Photogrammetry through shallow water. Australian Journal of Geodesy, Photogrammetry and Surveying 38: 25-38.

Fryer, J. G, & Kniest HT. (1985). Errors in depth determination caused by waves in through-water photogrammetry. Photogrammetric Record 11(66): 745–753.

Grenzdörffer, G. J., & Naumann M. (2016). Investigation on the possibilities of monitoring coastal changes including shallow under water areas with UAS photo bathymetry. The International Archives of the Photogrammetry, Remote Sensing and Spatial Information Sciences XLI-B1. DOI:10.5194/isprsarchives-XLI-B1-843-2016.

Harris, W. D., & Umbach M. J. (1972). Underwater mapping. PhotogrammetricEngineering 38: 765–772.

Harwin, S. & Lucieer, A. (2012). Assessing the accuracy of georeferenced point clouds produced via multi-view stereopsis from unmanned aerial vehicle (UAV) imagery. Remote Sensing 4: 1573-1599.

Hsu, P. H., & Wang, C. K. (2011). Acquiring Underwater DSM Using Close-Range Photogrammetry. In Proceeding 32nd Asian Conference on Remote Sensing 2011, 267-272.

James, M. R. & Robson, S. (2012). Straightforward reconstruction of 3D surfaces and topography with a camera: accuracy and geosciences application. Journal of Geophysical Research 117, F03017, doi: 10.1029/2011JF002289.

James, M. R., & Robson, S. (2014). Mitigating systematic error in topographic models derived from UAV and ground-based image networks. Earth Surface Processes and Landforms 39(10): 1413–20. DOI:10.1002/esp.3609.

Jia, D., Shao, X., Wang, H., & Zhou, G. (2010). Three-dimensional modeling of bank erosion and morphological changes in the Shishou bend of the middle Yangtze River. Advances in Water Resources 33: 348-360.

Kay, S., Hedley, J. D., & Lavender, S. (2009). Sun glint correction of high and low spatial resolution images of aquatic scenes: a review of methods for visible and near-infrared Wavelengths. Remote Sensing 1: 697–730. DOI:10.3390/rs1040697.

Lane, S. N., Widdison, P. E., Thomas, R. E., Ashworth, P. J., Best, J. L., Lunt, I. A., Sambrook Smith, G. H, Simpson, C. J. (2010). Quantification of braided river channel change using archival digital image analysis. Earth Surface Processes and Landforms 35: 971–985. DOI:10.1002/esp.2015.

Legleiter, C. J., & Kyriakidis P.C. (2008). Spatial prediction of river channel topography by kriging. Earth Surface Processes Landform 33(6): 841-867.

Lowe, D.G. (2004). Distinctive image features from scale-invariant keypoints. International Journal of Computer Vision 60: 91-110.

Mandlburger, G., Pfennigbauer, M., Wieser, M., Riegl, U., & Pfeifer, N. (2016). Evaluation of a novel UAV-borne topo-bathymetric laser profiler. The International Archives of the Photogrammetry, Remote Sensing and Spatial Information Sciences, Volume XLI-B1. DOI:10.5194/isprsarchives-XLI-B1-933-2016.

Marcus, W. A. (2012). Remote sensing of the hydraulic environment in gravel-bed rivers. In Gravel-bed Rivers: Processes, Tools, Environments, Church, M., Biron, P. and Roy, A. (Eds) Wiley-Blackwell, Chichester.

Monica, R.V., Rocio, B.G., Thomas, K., & Amanda, V. (2015). Automated Identification of River Hydromorphological Features Using UAV High Resolution Aerial Imagery. Sensors, 15: 27969-27989.

Mount, R. (2005). Acquisition of through-water aerial survey images: surface effects and the prediction of sun glitter and subsurface illumination. Photogrammetric Engineering and Remote Sensing 71 (12): 1407–1415. DOI:10.14358/PERS.71.12.1407.

Murase, T., Tanaka, M., Tani, T., Miyashita, Y., Ohkawa, N., Ishiguro, S., Suzuki, Y., Kayanne, H., & Yamano, H. (2008). A photogrammetric correction procedure for light refraction effects at a two-medium boundary. Photogrammetric Engineering & Remote Sensing 74: 1129–1136. DOI:10.14358/PERS.74.9.1129.

Nagata, N., Hosoda, T., & Muramoto, Y. (2000). Numerical analysis of river channel processes with bank erosion. Journal of Hydraulic Engineering, 126 (4): 243-252.

Neitzel, F. & Klonowski, J. (2011). Mobile 3D mapping with a low-cost UAV system. International Archives of the Photogrammetry, Remote Sensing and Spatial Information Sciences Vol. XXXVIII-I/C22, Conference on UAVs in Geomatics, Zurich, Switzerland.

Overstreet, B. T., & Legleiter, C. J. (2017). Removing sun glint from optical remote sensing images of shallow rivers. Earth Surface Processes and Landforms 42: 318-333. DOI: 10.1002/esp.4063.

Partama, I. G. Y., Kanno, A., Akamatsu, Y., Inui, R., Goto, M., & Sekine, M. (2017). A Simple and Empirical Refraction Correction Method for UAV-Based Shallow-Water Photogrammetry. proceedings of ICPRS 2017: 19th International Conference on Photogrammetry and Remote Sensing 19(4): 2778-2785.

Rosnell, T. & Honkavaara, E. (2012). Point cloud generation from aerial image data acquired by a quadrocopter type micro unmanned aerial vehicle and a digital still camera. Sensors 12: 453-480.

Sarretta, A., Pillon, S., Molinaroli, E., Guerzoni, S., & Fontolan, G. (2010). Sediment budget in the Lagoon of Venice, Italy. Continental Shelf Research 30: 934-949. DOI: 10.1016/j.csr.2009.07.002.

Smith, M., Vericat, D., & Gibbins, C. (2012). Through-water terrestrial laser scanning of gravel beds at the patch scale. Earth Surface Processes and Landforms 37: 411-421. DOI:10.1002/esp.2254.

Snavely, N., Seitz, S. M. & Szeliski, R. (2006). Photo tourism: exploring photo collections in 3D. ACM Transactions on Graphics 25 (3): 835-846.

Snavely, N., Seitz, S. M. and Szeliski, R. (2008). Modelling the world from internet photo collections. International Journal of Computer Vision 80 (12): 189-210.

Tewinkel, G. C. (1963). Water depths from aerial photographs. Photogrammetric Engineering 26: 1037–1042.

Turner, D., Lucieer, A. & Watson, C. (2012). An automated technique for generating georectified mosaics from ultra-high resolution unmanned aerial vehicle (UAV) imagery, based on Structure from Motion (SfM) point clouds. Remote Sensing 4: 1392-1410.

Ulrich, K., Rainer, B., & Konrad, H. (2004). Assessment of river habitat in Brandenburg, Germany. Limnologica, 34: 176-186.

Verhoeven, G., Doneus, M., Briese, Ch. & Vermuelen, F. (2012). Mapping by matching: a computer vision-based approach to fast and accurate georeferencing of archaeological aerial photographs. Journal of Archaeological Science 39: 2060-2070.

Vismara, R., Azzellino, A., Bosi, R., Crosa, G., & Gentili, G. (2001). Habitat suitability curves for brown trout (Salmo trutta fario L.) in the River Adda, Northern Italy: comparing univariate and multivariate approaches. Regulated Rivers: Research & Management 17: 37-50.

Webster, T., McGuigan, K., Collins, K., & MacDonald, C. (2014). Integrated river and coastal hydrodynamic flood risk mapping of the LaHave river estuary and town of Bridgewater, Nova Scotia, Canada. Water 6: 517-546. DOI:10.3390/w6030517.

Westaway, R. M., Lane, S. N., & Hicks, D. M. (2000). The development of an automated correction procedure for digital photogrammetry for the study of wide, shallow, gravel-bed Rivers. Earth Surface Processes and Landforms 25: 209–226. DOI:10.1002/(SICI)1096-9837 (200002)25:2<209::AID-ESP84>3.0.CO;2-Z.

Westaway, R. M., Lane, S. N., & Hicks, D. M. (2001). Remote sensing of clear-water, shallow, gravel-bed rivers using digital photogrammetry. Photogrammetric Engineering and Remote Sensing 67: 1271–1282.

Westoby, M. J., Brasington, J., Glasser, N. F., Hambrey, M. J. & Reynolds, J.M. (2012) Structure-from-Motion photogrammetry: a low cost, effective tool for geoscience applications. Geomorphology 179: 300-314.

Woodget, A. S., Carbonneau, P. E., Visser, F., & Maddock, I. P. (2015). Quantifying submerged fluvial topography using hyperspatial resolution UAS imagery and structure from motion photogrammetry. Earth Surface Processes and Landforms 40: 47–64. DOI:10.1002/esp.3613.

Appendix

Table 1. Fresnel reflectance of an air-water surface for p-polarized, s-polarized, and un-polarized light as a function of incidence angle.

Incidence angle [degrees]	Reflectance of p wave	Reflectance of s wave	Reflectance of unpolarised light
0	0.0205	0.0205	0.0205
1	0.0205	0.0205	0.0205
2	0.0204	0.0205	0.0205
3	0.0204	0.0206	0.0205
4	0.0203	0.0206	0.0205
5	0.0202	0.0207	0.0205
6	0.0201	0.0208	0.0205
7	0.0200	0.0209	0.0205
8	0.0199	0.0211	0.0205
9	0.0197	0.0213	0.0205
10	0.0195	0.0214	0.0205
11	0.0193	0.0216	0.0205
12	0.0191	0.0219	0.0205
13	0.0189	0.0221	0.0205
14	0.0186	0.0224	0.0205
15	0.0184	0.0227	0.0205
16	0.0181	0.0230	0.0206
17	0.0178	0.0234	0.0206
18	0.0174	0.0238	0.0206
19	0.0171	0.0242	0.0206
20	0.0167	0.0246	0.0207
21	0.0163	0.0251	0.0207
22	0.0159	0.0256	0.0208
23	0.0155	0.0261	0.0208
24	0.0150	0.0267	0.0209
25	0.0146	0.0273	0.0210
26	0.0141	0.0280	0.0210
27	0.0136	0.0287	0.0211
28	0.0131	0.0294	0.0213
29	0.0126	0.0302	0.0214
30	0.0120	0.0311	0.0215
31	0.0114	0.0320	0.0217
32	0.0109	0.0330	0.0219
33	0.0103	0.0340	0.0221
34	0.0097	0.0351	0.0224
35	0.0091	0.0362	0.0227
36	0.0084	0.0375	0.0230
37	0.0078	0.0388	0.0233
38	0.0072	0.0402	0.0237
39	0.0065	0.0417	0.0241
40	0.0059	0.0434	0.0246

41	0.0053	0.0451	0.0252
42	0.0046	0.0469	0.0258
43	0.0040	0.0489	0.0264
44	0.0034	0.0510	0.0272
45	0.0028	0.0532	0.0280
46	0.0023	0.0556	0.0290
47	0.0018	0.0582	0.0300
48	0.0013	0.0610	0.0311
49	0.0009	0.0639	0.0324
50	0.0005	0.0671	0.0338
51	0.0003	0.0705	0.0354
52	0.0001	0.0741	0.0371
53	0.0000	0.0781	0.0390
54	0.0000	0.0823	0.0412
55	0.0002	0.0868	0.0435
56	0.0006	0.0917	0.0462
57	0.0012	0.0970	0.0491
58	0.0019	0.1027	0.0523
59	0.0030	0.1088	0.0559
60	0.0043	0.1155	0.0599
61	0.0060	0.1226	0.0643
62	0.0080	0.1303	0.0692
63	0.0105	0.1387	0.0746
64	0.0136	0.1477	0.0807
65	0.0172	0.1575	0.0873
66	0.0214	0.1681	0.0948
67	0.0265	0.1796	0.1030
68	0.0324	0.1921	0.1122
69	0.0393	0.2056	0.1224
70	0.0473	0.2202	0.1337
71	0.0566	0.2361	0.1464
72	0.0674	0.2534	0.1604
73	0.0798	0.2721	0.1760
74	0.0942	0.2925	0.1933
75	0.1108	0.3146	0.2127
76	0.1298	0.3387	0.2342
77	0.1517	0.3648	0.2583
78	0.1769	0.3932	0.2850
79	0.2057	0.4241	0.3149
80	0.2389	0.4576	0.3482
81	0.2769	0.4941	0.3855
82	0.3204	0.5337	0.4271
83	0.3704	0.5767	0.4736
84	0.4277	0.6235	0.5256
85	0.4934	0.6742	0.5838
86	0.5687	0.7293	0.6490
87	0.6552	0.7890	0.7221
88	0.7546	0.8538	0.8042
89	0.8687	0.9240	0.8964
90	1.0000	1.0000	1.0000